Remote Sensing of Environment 233 (2019) 111348

Contents lists available at ScienceDirect

Remote Sensing of Environment

journal homepage: www.elsevier.com/locate/rse

High-resolution DEM generation from spaceborne and terrestrial remote sensing data for improved volcano hazard assessment — A case study at Nevado del Ruiz, Colombia

Fanghui Deng[a,*], Mel Rodgers[a], Surui Xie[a], Timothy H. Dixon[a], Sylvain Charbonnier[a], Elisabeth A. Gallant[a], Cristian Mauricio López Vélez[b], Milton Ordoñez[b], Rocco Malservisi[a], Nicholas K. Voss[a], Jacob A. Richardson[c,d]

[a] School of Geosciences, University of South Florida, Tampa, FL 33620, United States
[b] Department of Geological Hazards, Colombian Geological Service, Manizales, Colombia
[c] Planetary Geology, Geophysics and Geochemistry Lab, NASA Goddard Space Flight Center, Greenbelt, MD 20771, United States
[d] Department of Astronomy, University of Maryland, College Park, MD 20742, United States

ARTICLE INFO

Edited by Jing M. Chen

Keywords:
Nevado del Ruiz
Digital elevation model
TanDEM-X
InSAR
Terrestrial radar interferometry
Structure from motion
DEM fusion
Volcanic flow modeling

ABSTRACT

Volcanoes with rugged terrain remain a challenging target for generating high-resolution digital elevation models (DEMs), especially in tropical areas with frequent cloud cover. Using Nevado del Ruiz volcano as an example, we combined DEMs from the TanDEM-X (TDX) satellite mission, terrestrial radar interferometry (TRI), and Structure from Motion (SfM), to generate a new DEM with 10-m spatial resolution. This is the first study combining satellite radar, ground-based radar, photography, and freely available global DEMs to generate a high-resolution DEM without data gaps. TDX data from ascending and descending orbits were combined to generate the base DEM. Instead of using a raster format to fuse DEMs generated from different data sets with different resolutions, we developed a methodology based on 3-D point clouds: 1) re-georeference the 5-m TRI and ~1-m SfM DEMs to the 10-m TDX DEM using the iterative closest point (ICP) algorithm to minimize the horizontal and vertical discrepancy between DEMs; then 2) merge the multiple point clouds to generate a final DEM without data gaps using an adaptive algorithm that uses two search distances to smooth the transition at the edges of different data sets. We assess the new 10-m DEM by comparing simulated inundation zones obtained with two volcano flow models, LaharZ (for lahars) and VolcFlow (for pyroclastic flows), and find significant differences with respect to the 30-m SRTM DEM. Our LaharZ simulation over the new DEM shows a longer lahar run-out distance. For pyroclastic flows, the VolcFlow simulation over the new DEM produces highly channelized flows over the steep portions of a river channel and gives a larger extent of thicker deposits compared to those obtained with the 30-m SRTM DEM. Quantitative and qualitative geomorphic analysis suggests that up-to-date DEMs with high spatial resolution (~ 10 m or even better) need to be generated to improve volcano hazard assessment for active volcanoes.

1. Introduction

With the rapid development of satellite remote sensing techniques, digital elevation models (DEMs) have become widely available. In particular, DEMs based on data from the Shuttle Radar Topography Mission (SRTM) (Rabus et al., 2003; Farr et al., 2007), the Advanced Spaceborne Thermal Emission and Reflection Radiometer (ASTER) mission (Tachikawa et al., 2011), the ALOS Panchromatic Remote-sensing Instrument for Stereo Mapping (PRISM) mission (Tadono et al., 2014), and the TanDEM-X (TDX) mission (Krieger et al., 2007) provide global coverage and are sufficient for many applications (e.g., Ludwig and Schneider, 2006; Toutin, 2008; Ehsani and Quiel, 2008; Hayakawa et al., 2010; Yang et al., 2015). However, radar interferometry (e.g., SRTM and TDX) is challenged by high relief terrain, which causes both shadowing and "layover" (distortion associated with the imaging geometry of side-looking radars) (e.g, Eineder, 2003; Farr et al., 2007; Kubanek et al., 2015b). Stereo-optical techniques (e.g., ASTER and ALOS PRISM) are challenged by cloud cover, especially in the tropics (e.g., Hirano et al., 2003; Toutin, 2004). Volcanoes usually have high relief and many are located in tropical regions (Global Volcanism

* Corresponding author.
E-mail address: fanghuideng@mail.usf.edu (F. Deng).

https://doi.org/10.1016/j.rse.2019.111348
Received 26 July 2018; Received in revised form 22 July 2019; Accepted 23 July 2019
Available online 13 August 2019

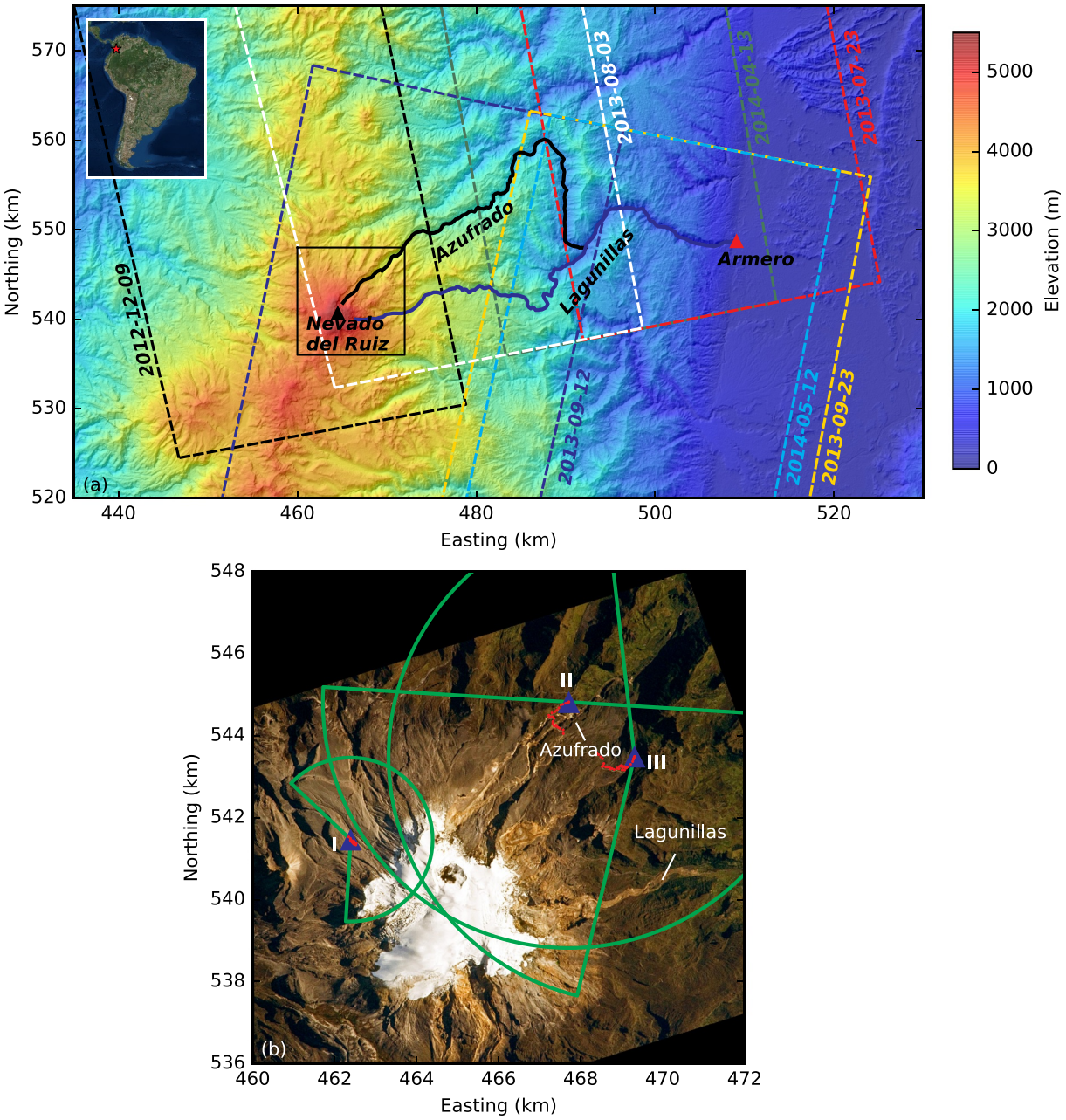

Fig. 1. (a) Topographic map of the study area based on the 30-m SRTM DEM. The black and red triangles indicate the location of the crater of Nevado del Ruiz volcano and the city of Armero. Solid lines indicate the Azufrado (black) and Lagunillas (blue) drainage channels that conveyed lahars to Armero, causing the Armero tragedy in 1985 (Pierson et al., 1990). Dashed-lined polygons show the extent of TDX data (Table 1) used for DEM generation, with acquisition dates labeled. The solid-lined black box shows location of (b). Inset map shows the location of Nevado del Ruiz volcano (red star) in South America. (b) Optical image of Nevado del Ruiz. White areas near the crater are ice and snow. Blue triangles are mounting locations of the terrestrial radar. Green arcs show the extent of radar-scanned areas. Red dots are GPS-RTK points. The optical image (Astronaut photograph ISS023-E-27737, 2010) was acquired on April 23, 2010 with a digital camera. (For interpretation of the references to colour in this figure legend, the reader is referred to the web version of this article.)

Program, 2013). The net effect is that volcanoes remain one of the few remaining gaps in the pool of so-called "global" high resolution DEMs, with voids, poorly interpolated data, and erroneous values. These problems limit the accuracy of hazard assessment based on flow models, e.g., lahars and pyroclastic flows, typically the major sources of fatalities from volcanic eruptions.

Nevado del Ruiz is one of the most active volcanoes in the Andes, located in the Cordillera Central, Colombia (Global Volcanism Program, 2013), and caused one of the deadliest volcanic disasters in recent history. On November 13, 1985, a relatively small eruption (with a Volcano Explosivity Index (VEI) of 3) triggered enormous lahars, killing > 20,000 people in the town of Armero (Fig. 1a) and over 3000 people in surrounding communities (Lowe et al., 1986; Naranjo et al., 1986; Schuster and Highland, 2001). Meltwater from a glacier capping the volcano summit (Fig. 1b) was a main contributor to the lahars (Lowe et al., 1986; Naranjo et al., 1986). The meltwater was mainly produced by the interaction between pyroclastic flows and the snow and ice (Pierson et al., 1990).

Activity at Nevado del Ruiz has increased over the last few years, causing a serious concern for future lahar generation. From 2010 to present, increased seismicity, surface deformation, ash plumes and gas emissions have been observed. In September 2010, seismicity notably increased, prompting authorities to raise the alert to Level III (Yellow) on a four-level scale (Wunderman, 2012; Londoño, 2016; Vargas et al.,

2017). SO_2 emissions have increased since 2010, reaching over 20,000 tons/day in 2012, with high values (generally 20,000–30,000 tons/day) continuing to the present time (Londoño, 2016). InSAR (Interferometric Synthetic Aperture Radar) observations indicate surface inflation rates of 3–4 cm/yr starting around the end of 2011 (Lundgren et al., 2015). A new lava dome has been observed to extrude near the summit of the volcano beginning in September 2015 (Londoño, 2016). Observations by the COSMO-SkyMed satellite suggest an estimated pseudo-volume (deformation observed by InSAR from a single orbit cannot reconstruct the real 3-D world) of the lava dome of 12,000 m^3 (SGC, Servicio Geológico Colombiano, 2015; Londoño, 2016).

A DEM is a key requirement for prediction of volcanic mass flows (e.g., lava flows, pyroclastic flows, lahars). Existing research shows that resolution and accuracy of the DEM can affect the performance of volcanic mass flow models, the simulated flow paths, run outs and thicknesses (e.g., Stevens et al., 2003; Hubbard et al., 2007; Huggel et al., 2008; Capra et al., 2011; Kubanek et al., 2015a; Turner et al., 2017; Charbonnier et al., 2018). Huggel et al. (2008) evaluated ASTER and SRTM DEMs for lahar modeling and suggested that in most cases the SRTM DEM represents the actual topography more reliably than the ASTER DEM, especially with regard to the main drainages. Capra et al. (2011) reproduced past block-and-ash flows at Colima volcano (Mexico) over DEMs with different resolutions (5, 10, 30, 50, and 90 m) using the Titan2D code (Patra et al., 2005). They suggested that in the particular case of rugged topography, a DEM with resolution of 5–10 m should be acquired in order to obtain confident simulation results.

The DEMs currently freely available that cover Nevado del Ruiz volcano and the city of Armero include the 30-m SRTM DEM, 30-m ASTER DEM, ALOS World 3D 30 m (AW3D30) DEM, and 90-m TDX DEM (Fig. 2). Considering the data gaps in SRTM DEM (Fig. 2a, Text S1), the low accuracy in ASTER DEM (Fig. 2e), and the relatively low resolutions (30 m and 90 m) of all of them, a new DEM with much higher resolution is necessary to improve volcanic hazard assessment for Nevado del Ruiz and its surrounding regions.

The current availability of various remote sensors for topographic data collection provides an opportunity to apply DEM fusion methods to improve the quality of DEM products. The input DEMs for fusion can be from the same sensor (e.g., Sansosti et al., 1999; Crosetto, 2002; Deo et al., 2015), or from different sensors (e.g., Gamba et al., 2003; Gelautz et al., 2003; Kääb, 2005; Reinartz et al., 2005; Karkee et al., 2008; Papasaika et al., 2011; Kolzenburg et al., 2016). Among the above DEM fusion studies, the resolution of input DEMs was the same or relatively close, and the authors mainly focused on vertical corrections (e.g., Van Niel et al., 2008; Hirt et al., 2010; Jarihani et al., 2015). In this paper, we develop a methodology to fuse DEMs with different horizontal and vertical accuracies and resolutions (~1 m to 10 m).

In this study, TDX data, terrestrial radar interferometry (TRI) and structure from motion (SfM) were combined to generate a 10-m DEM covering the area from Nevado del Ruiz volcano to the city of Armero (Fig. 1a). Ascending and descending TDX data were used to generate the base DEM. TRI and SfM data were used to fill in several data gaps in the critical Azufrado channel (Fig. 1b). DEM re-georeferencing and merging were performed in 3-D point cloud format. We evaluated the impact of the new DEM for volcanic hazard assessment by comparing simulated inundation zones of lahars and pyroclastic flows using the 30-m SRTM DEM and our new 10-m DEM.

2. DEM generation for individual data sets

2.1. Satellite interferometry using TanDEM-X SAR data

The German Aerospace Center (DLR) has generated global 90-m, 30-m and 12-m DEMs from SAR data acquired by their TanDEM-X (TDX) mission (Krieger et al., 2007; Hoffmann et al., 2016), a mission operated together with the partners EADS Astrium GmbH and Infoterra GmbH in a Public Private Partnership consortium. The TDX satellite flies in tandem with the TerraSAR-X satellite, allowing a bistatic mode whereby one satellite illuminates the earth and both satellites receive

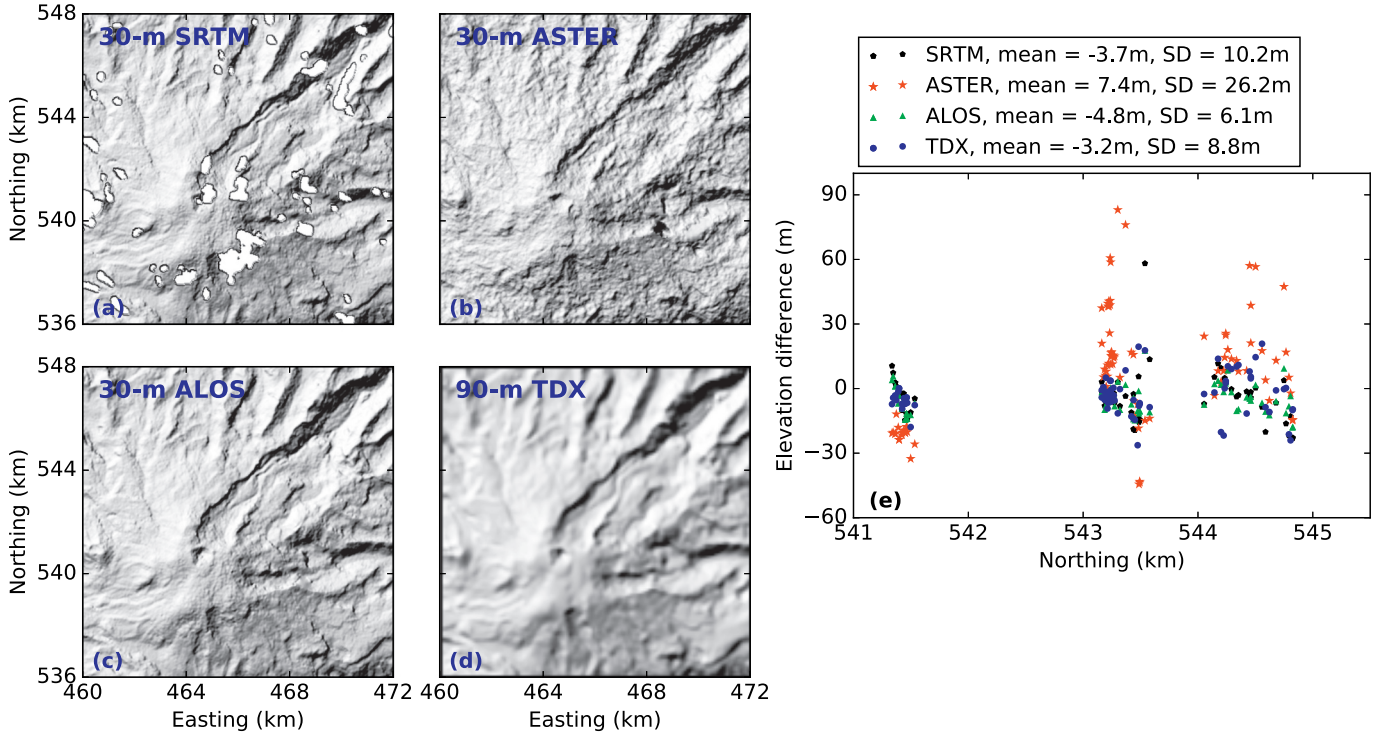

Fig. 2. Four freely available DEMs of Nevado del Ruiz volcano. (a) - (d) are hillshade maps of the 30-m SRTM DEM, 30-m ASTER DEM, 30-m ALOS DEM, and 90-m TDX DEM, respectively. Note the data gaps in the SRTM DEM (version: SRTM 1 Arc-Second Global; Digital Object Identifier (DOI) number: /https://doi.org/10.5066/F7PR7TFT). (e) Elevation difference between the above four DEMs and our GPS-RTK measurements (Fig. 1b). Mean and standard deviation (SD) values are indicated for each DEM.

the return signal (Krieger et al., 2007; Zink et al., 2008). The 90-m TDX DEM is freely available. Scientific users can propose to access the 12-m and 30-m TDX DEM products and the SAR images to generate their own DEM. Special attention should be paid when applying DLR's TDX DEM products in active volcanoes. In their DEM generation, the elevation value for a given pixel is the weighted average of height values from multiple DEM scenes (Hoffmann et al., 2016). Although height inconsistency was evaluated and provided along with the DEM product, it is not used in calculating the final DEM (Hoffmann et al., 2016). Topographic changes due to volcanic activity can reach meters to tens of meters (e.g., Charbonnier and Gertisser, 2009; Poland, 2014; Albino et al., 2015; Kubanek et al., 2015a; Arnold et al., 2016; Rossi et al., 2016; Kubanek et al., 2017). Possible artefacts due to large topographic changes should be kept in mind when using DLR's TDX DEM products in active volcanoes.

Between 1991 and February 2012 intermittent high-frequency seismic events (earthquake swarms) were recorded at the Nevado del Ruiz volcano, but no ash emissions were observed. During 2012–2015, several ash emission and ashfall activities were observed (Global Volcanism Program, 2017). Surface deformation observed by InSAR data suggests inflation rates of 3–4 cm/yr during this period (Lundgren et al., 2015). The topographic changes due to these volcanic activities have much smaller magnitude compared to the TDX DEM accuracy (e.g., < 4-m relative vertical accuracy for the 12-m TDX DEM product; Fig. 3), therefore are not considered during our DEM fusion process. The crater area may have significant topographic change. But none of our data sets have good coverage there.

InSAR (Interferometric Synthetic Aperture Radar) is widely used for DEM generation, allowing for all-weather, day-and-night observations (e.g., Zebker and Goldstein, 1986; Rufino et al., 1998; Lu et al., 2000; Farr et al., 2007; Osmanoglu et al., 2014; Zhou et al., 2015; Rossi et al., 2016). We used the state-of-the-art InSAR method (e.g., Poland, 2014; Jiang et al., 2014; Avtar et al., 2015; Kubanek et al., 2017; Arnold et al., 2017) for DEM generation using the TDX data. We generated the differential interferogram by subtracting a simulated interferogram (using an external DEM as reference) from the real TDX interferogram. We unwrapped the above residual phase and converted the unwrapped phase to elevation difference Δh. Then Δh was added back to the reference DEM. This can reduce phase unwrapping error compared to unwrapping the initial TDX interferogram directly, especially for mountainous areas like volcanoes.

SAR data were processed using the GAMMA software (Werner et al., 2000). Four (range) by four (azimuth) multilooking was used to reduce speckle noise (Porcello et al., 1976; Lee et al., 1994). The 30-m SRTM DEM (version: SRTM 1 Arc-Second Global; Digital Object Identifier (DOI) number: /https://doi.org/10.5066/F7PR7TFT) was used to provide ground control points and to geo-reference the results from radar coordinates to map coordinates. The 30-m SRTM DEM was gap-filled with the 30-m AW3D DEM before data processing (Text S1), i.e., for a certain pixel in the SRTM DEM, if its value is void (NaN) then the height value is taken directly from the 30-m AW3D to replace it. Unless otherwise stated, the SRTM DEM used in this paper is gap-filled. The TDX DEMs were geo-referenced to the SRTM DEM at about 1.5-pixel (10 × 10 m/pixel) horizontal accuracy (Table 2), based on the TDX orbital information and the co-registration of the real (TDX) and simulated (based on SRTM DEM) SAR intensity images (Text S2; GAMMA Remote Sensing AG, 2008). Residual ramps remained in the elevation difference between the TDX DEMs and SRTM DEM (Fig. S1a), which could be due to processing errors. The ramp was fitted with a quadratic polynomial using the least-squares method (e.g., Poland, 2014; Arnold et al., 2016), and removed from the original TDX DEMs (Fig. S1b). The generated TDX DEMs have a spatial resolution of 10 × 10 m. The horizontal and vertical datums of all DEMs in this paper are in or are transformed to the WGS84 coordinate system. The heights are ellipsoidal heights. The conversion between different coordinate systems (e.g, orthometric height to ellipsoid height) is achieved by using VDatum software (https://vdatum.noaa.gov/) developed by the National Oceanic and Atmospheric Administration (NOAA) (Milbert, 2002; Parker et al., 2003).

The TDX height uncertainty is estimated empirically by checking the elevation difference between TDX DEMs acquired at different times (e.g., Poland, 2014; Arnold et al., 2016; Kubanek et al., 2017). Topography should have almost no change over the time span. Taking TDX DEM 2012-12-09 as a reference, the standard deviation of elevation difference for TDX DEMs 2013-08-03 and 2013-09-12 at the summit area (mountainous terrain) is ~ 6 m (Fig. 3). The relatively large uncertainty of DEM 2013-08-03 is probably related with its steep incidence angle (Table 2).

To reduce the effect of geometric distortions inherent in SAR images, TDX DEMs generated from ascending and descending orbits are combined (e.g., Sansosti et al., 1999; Farr et al., 2007; Deo et al., 2014; Deo et al., 2015). Merging multiple TDX DEMs allows us to define standards to evaluate the reliability of each height value. Coherence is a widely used parameter for this (e.g., Sansosti et al., 1999; Deo et al., 2014; Deo et al., 2015), since in general high coherence in the SAR interferogram corresponds to low noise. In some previous studies, geometric parameters (e.g., satellite heading angle, incidence angle, local slope and aspect, baseline) are also considered as thresholds or

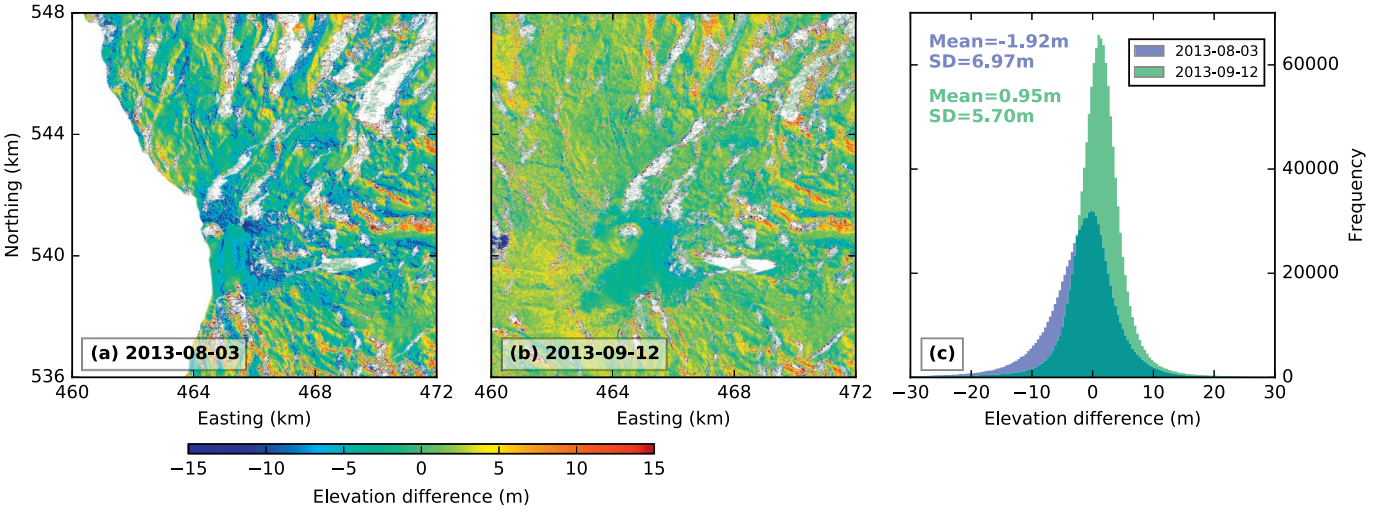

Fig. 3. Elevation difference of TDX DEMs 2013-08-03 (a) and 2013-09-12 (b) relative to 2012-12-09. (c) Corresponding histograms of (a) and (b). Mean and SD are calculated and labeled.

used to mask out or interpolate shadow and layover areas (e.g., Eineder, 2003; Deo et al., 2014). Another candidate for assessment of the TDX DEM is the elevation difference Δh, the difference between the TDX DEM and the reference DEM (SRTM DEM in our case). Assessing Δh is an effective way to detect errors in DEMs, e.g., phase unwrapping errors, since the SRTM DEM has high vertical accuracy (16 m absolute and 6 m relative vertical accuracy (Farr et al., 2007)) and the TDX DEM is supposed to have even higher vertical accuracy (e.g., < 10 m absolute and ⩽4 m relative vertical accuracy for the DLR's 12-m product (Hoffmann et al., 2016)). In this paper, we used coherence C and elevation difference Δh (Table 2) as thresholds. Geometric parameters were not used 1) to avoid additional artefacts (e.g., the calculated local slope and aspect may be uncertain in areas with steep slopes); and 2) since a relatively high coherence threshold can generally mask out layover and shadow areas (Fig. S2).

Threshold values for coherence C and elevation difference Δh are determined by mean and standard deviation (SD) values (Table 2). 0.6 (the lowest average coherence in Table 2) is used for C to guarantee reliable phase unwrapping and good data coverage. Three times the average SD (Table 2), 34.86 m, is used for Δh. This value is empirical and smaller than the minimum height of ambiguity H_oA (change in topographic height corresponding to a phase change of 2π or 1π) (Table 1). This can reduce height errors due to phase unwrapping errors, which will result in height errors of $N \times H_oA$ (N is a non-zero integer). At the same time it can take full advantage of the TDX DEMs considering that they are supposed to have higher vertical accuracy than the SRTM DEM. For a certain location (pixel) covered by multiple TDX DEMs, only elevation values with coherence higher than C and elevation difference lower than Δh are considered (averaged) in the final DEM (Fig. S3). Note that the threshold values are empirical. Different values could be used depending on application. For example, for a looser constraint, we can use a lower coherence and a higher elevation difference as thresholds. For active volcanoes, a higher Δh should be considered locally if volcanic activity results in large topographic changes (e.g., similar magnitude to height of ambiguity). The merged TDX DEM (Fig. 4a) has a spatial resolution of 10 by 10 m. The SD of the elevation difference between the merged TDX DEM and the SRTM DEM is ~ 11 m (Fig. 4b).

2.2. Terrestrial radar interferometry (TRI)

Parts of the volcano have extremely steep slopes, especially in the upper reaches of the edifice which are cut by deep valleys east of Nevado del Ruiz volcano (e.g., the Azufrado channel). These are not well represented in the merged TDX DEM, reflecting the difficulty of applying satellite SAR techniques in high relief terrain. Terrestrial radar interferometry (TRI) has a different imaging geometry that can fill some of these gaps. TRI uses a scanning radar to measure the amplitude and phase of a backscattered microwave signal. It can generate high-resolution elevation and displacement maps (e.g., Strozzi et al., 2012; Dixon et al., 2012; Voytenko et al., 2015; Caduff et al., 2015; Xie et al., 2016, 2018, 2019). TRI provides a more flexible and reliable way to generate DEMs in steep-slope terrain, but field work is needed, and the spatial coverage of TRI is much smaller than satellite interferometry.

Two TRI surveys were conducted, in February and December 2015. The TRI we used is GAMMA's portable radar (Fig. S4, Werner et al., 2008). It is a real aperture radar operating at Ku-band (1.74 cm wavelength). The TRI has one transmitting antenna and two receiving antennas, which allow for mapping of topography with a single scan (Strozzi et al., 2012). The resolution of range measurements is ~1 m. Azimuth resolution is limited by the antenna beam width (0.4°) and hence varies linearly with slant range, e.g., ~7 m at 1 km distance, ~14 m at 2 km distance for a single scan. To reduce noise in the azimuth direction, we reduced the angular rotation step to 0.1° to increase the number of azimuth samples and enable azimuth averaging, assuming azimuth noise decreases as the number of samples increases. This improves the effective azimuth resolution - the practical improvement would depend on the amplitude of the backscattered signal.

The TRI instrument was deployed at three locations to image the upper slopes of the volcano (Fig. 1b). Data processing with TRI data to generate a DEM is very similar to satellite InSAR. Main steps include interferogram generation, phase unwrapping, converting unwrapped phase to height and geocoding (converting radar coordinate to map view). At each TRI location, DEMs generated from multiple radar scans were averaged to generate a final DEM. Details of TRI data processing for DEM generation are given in Strozzi et al. (2012) and Xie et al. (2019).

GPS-RTK (Real-time kinematic) measurements (Fig. 1b) were also carried out using a Trimble R10 receiver. The GPS data were post-processed with Trimble CenterPoint RTX Post-Processing service (https://www.trimblertx.com/UploadForm.aspx). Decimeter-level precision was achieved in the horizontal and vertical components. GPS measurements (List S1) were used to convert unwrapped phases to elevation values, and to perform preliminary projection of results from radar coordinates to map coordinates. Given that the GPS measurements are not evenly distributed, further geo-referencing is needed when merging the TRI DEMs into the TDX DEM.

Three DEMs, corresponding to the three TRI locations (Fig. 1b), were generated and re-sampled to 5-m by 5-m resolution (Fig. 5). The TRI DEMs have a smaller spatial extent compared to the scanned areas. One reason is that the strength of the radar signal decreases with distance. Some of the far-field regions imaged by the radar have high noise and were therefore removed during data processing. Another reason is that the radar signal in some regions is shadowed by steep slopes and vertical cliffs.

Table 1
Information describing the TDX SAR data pairs used in this study. All SAR data are in StripMap mode (Eineder et al., 2003). Data coverage is indicated in Fig. 1a. The distance between the two satellites (or orbits) in the plane perpendicular to the orbit is called the interferometer baseline. Its projection perpendicular to the slant range is the perpendicular baseline, and the projection parallel to the slant range is the parallel baseline. Height of ambiguity H_oA in the case of the bistatic mode is calculated based on $H_oA = \lambda R sin\theta / B_\perp$ (Martone et al., 2012; Rizzoli et al., 2017), where λ is the radar wavelength (3.1 cm), R is the slant range (~700 km), θ is the incidence angle, and $B_\perp$ is the perpendicular baseline.

Acquisition date (year-month-day)	Orbit	Parallel Baseline (meter)	Perpendicular Baseline (meter)	Incidence angle (degree)	Height of Ambiguity (meter)	Pixel spacing (meter)	
						Slant-range	Azimuth
2012-12-09	Ascending	124.9	110.4	46.7	158	1.4	2.2
2013-07-23	Ascending	71.8	93.4	32.1	125	1.4	1.7
2013-08-03	Ascending	59.9	32.0	29.7	347	1.4	2.0
2014-04-13	Ascending	158.9	29.6	31.0	372	1.4	2.2
2013-09-12	Descending	221.7	97.2	42.7	150	1.4	2.2
2013-09-23	Descending	171.0	83.8	40.4	167	1.4	2.0
2014-05-12	Descending	134.2	65.3	40.6	217	0.9	2.0

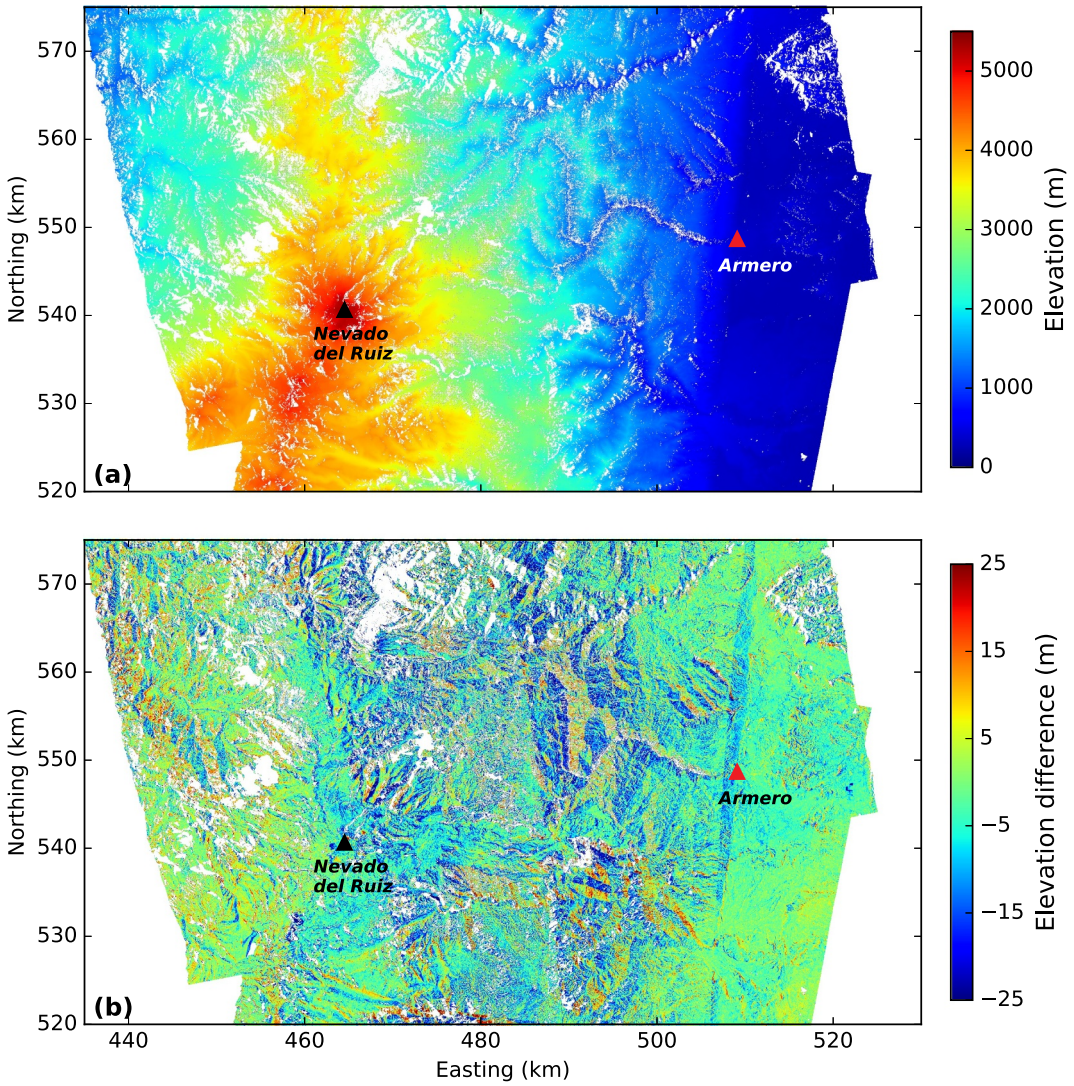

Fig. 4. (a) Merged TDX DEM covering area from Nevado del Ruiz volcano (black triangle) to the city of Armero (red triangle). (b) Elevation difference between the merged DEM and SRTM DEM. White areas mean data gaps. Mean and SD values of the elevation difference map are −2.18 m and 10.88 m, respectively. (For interpretation of the references to colour in this figure legend, the reader is referred to the web version of this article.)

2.3. Structure from motion (SfM)

Data gaps still existed in some of the deeper valleys due to observation geometry limitations in both satellite and terrestrial radars (Fig. 7a, d, e). We filled some of these gaps with photos taken by mid-high-end consumer digital cameras, including both single-lens reflex (DSLR) and point-and-shoot (compact) cameras. We used these photos and the Structure from Motion (SfM) technique to generate a geo-referenced dense point cloud. SfM is a photogrammetry technique that creates a 3D representation of an object or terrain from multiple overlapping 2D images (Westoby et al., 2012). The main difference between SfM techniques and traditional photogrammetry techniques is that SfM methods simultaneously solve for camera position (location and orientation) and 3D features, hence a priori information on camera locations is not needed (James and Robson, 2012; Westoby et al., 2012; Smith et al., 2016).

Approximately 2000 ground-based photos were taken during the two field campaigns mentioned above, focusing on some of the steep ravine areas of the Azufrado river channel. Drone based photography was attempted, but due to operational problems resulting from the high elevation and strong winds, only a few usable images were obtained.

Ground Control Points (GCPs) are necessary to accurately geo-reference the DEM. Notable natural and man-made features were used as GCPs. Position information was obtained using both a Trimble R10 receiver with RTK corrections (Fig. 1b), and a handheld GPS. Due to poor visibility conditions and the challenge of working in very steep and incised terrain, many of the GCPs were not identifiable in the SfM DEM, resulting in only 4 high-precision (measured by GPS-RTK, decimeter-level spatial and vertical precision) and 3 low-precision (measured by handheld GPS, ~ 10-m spatial and vertical precision) GCPs (Fig. 6a) visible in the model. Due to the lack of available GCPs, all 4 of these high-precision points were used for geo-referencing. The 3 low-precision GCPs were used for model validation in both horizontal and vertical directions. The transect survey using GPS-RTK (Fig. 1b, Fig. 6a) along a road section was compared to the SfM model for validation in the vertical direction (Fig. 6b).

Data processing for SfM consists of a multi-step process using Agisoft PhotoScan (http://www.agisoft.com/) to create a dense, geo-referenced point cloud, and CloudCompare (CloudCompare (version 2.9), 2017) for post-processing. Processing steps in Agisoft consisted of 1) initial photograph feature matching, alignment and bundle adjustment to create sparse point cloud; 2) review and refinement of badly aligned photographs - in this stage the addition of manually placed markers was essential to overcome the problems associated with limited

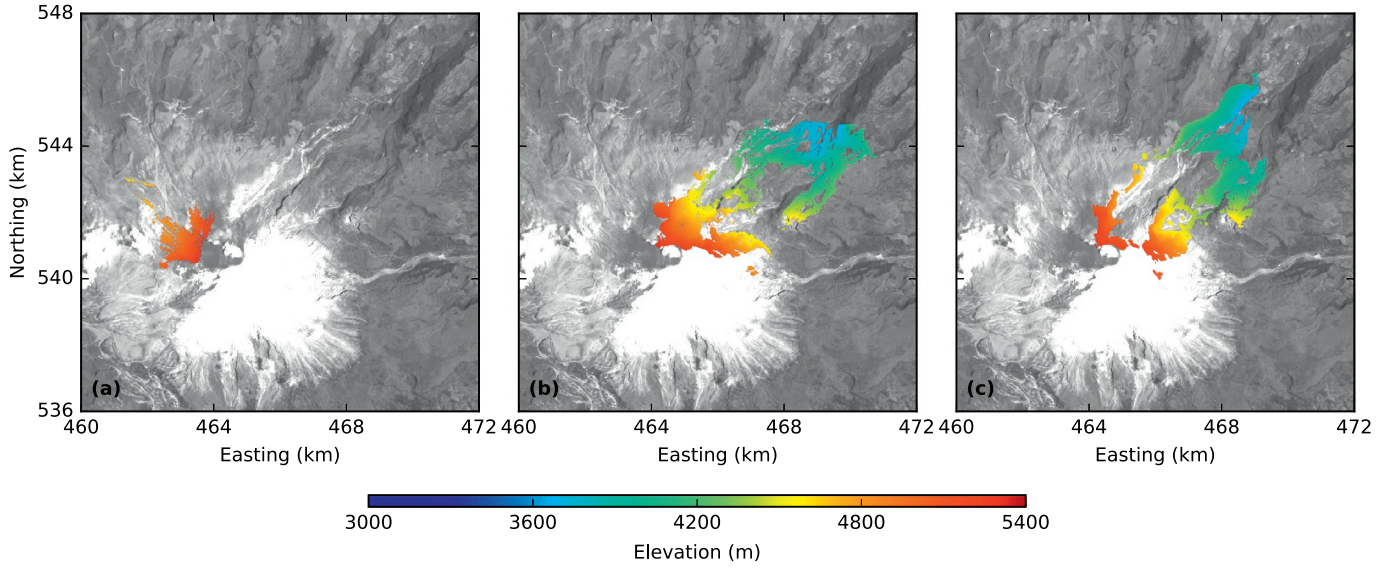

Fig. 5. TRI DEMs overlain on a Landsat-8 image acquired on 2015-09-24. (a), (b) and (c) correspond to data obtained at TRI location I, II and III (Fig. 1b) respectively.

overlap in some areas; 3) addition of GCPs and geo-referencing of the SfM DEM; and 4) creation of the dense point cloud. Ground acquisition of photographs in this environment was difficult due to steep slopes and abrupt elevation changes. Hence, in some areas, optimal photographic coverage was not possible, resulting in limited overlap and missed GCPs. Weather conditions (poor visibility due to heavy low cloud) also contributed to reduced image quality and difficulty in image matching. Once the dense point cloud was created in Agisoft it was then exported to CloudCompare for: 1) cleaning and refinement of dense point cloud; 2) gridding and generation of the final DEM. To reduce outliers and artefacts due to mismatching, the point cloud was cleaned using Statistical Outlier Remover and Noise filtering tools (CloudCompare user manual, 2015).

The average and SD of the elevation difference between the SfM DEM and the GPS-RTK measurements (blue dots in Fig. 6b) are −0.9 m and 5.7 m, respectively. Comparison between three GCPs taken with a handheld GPS and those corresponding points in the SfM DEM gives an average of 17.3 m in the northing, −18.9 m in the easting and 12.6 m in the vertical (Table 3, yellow dots in Fig. 6b). The low precision of the handheld GPS must be taken into consideration when assessing the error in the SfM DEM. The difference between the handheld GPS measurement and the SfM DEM are consistent in their sign in both the horizontal and vertical directions (Table 3), suggesting internal consistency within the SfM DEM.

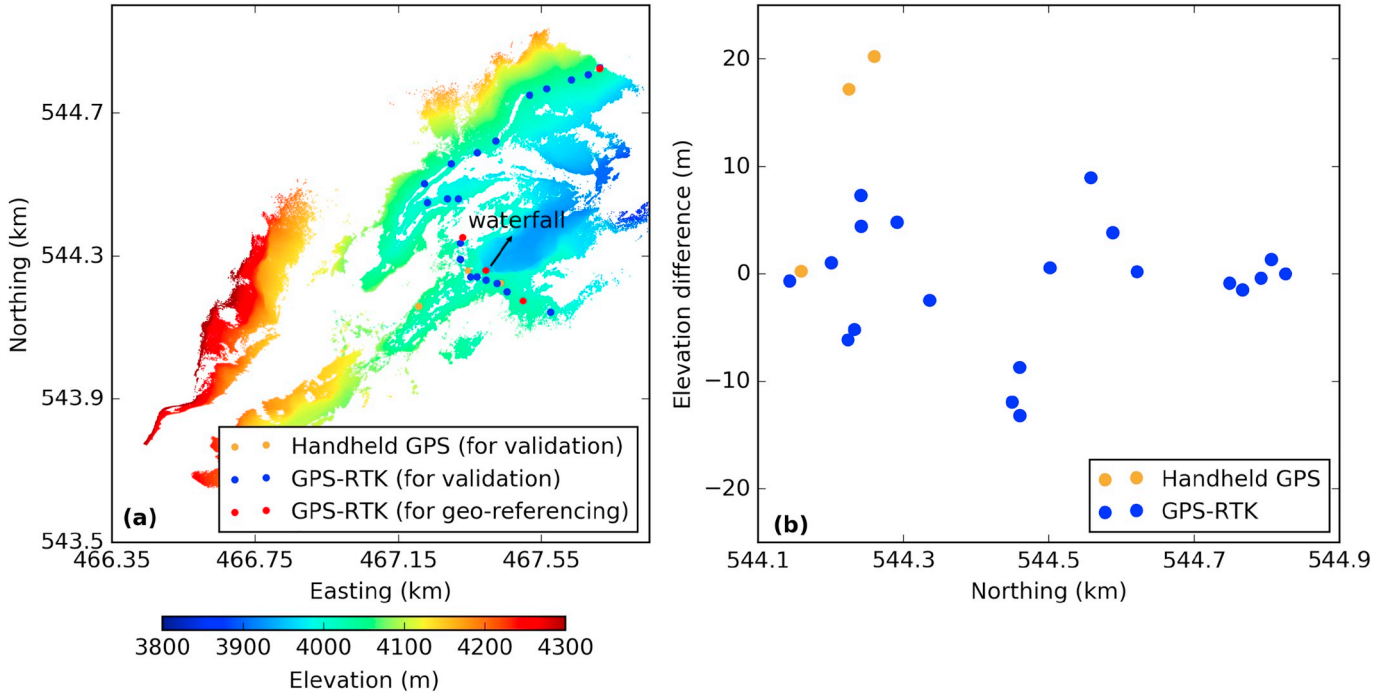

Fig. 6. (a) 2-D view of SfM point cloud colored with elevation values. Colored dots are GPS measurements. Note that one GPS-RTK measurement is located at the head of the waterfall (a local landmark on the pathway of the 1985 lahars) in the Azufrado channel (Fig. 7). (b) Elevation difference between the SfM DEM and GPS measurements.

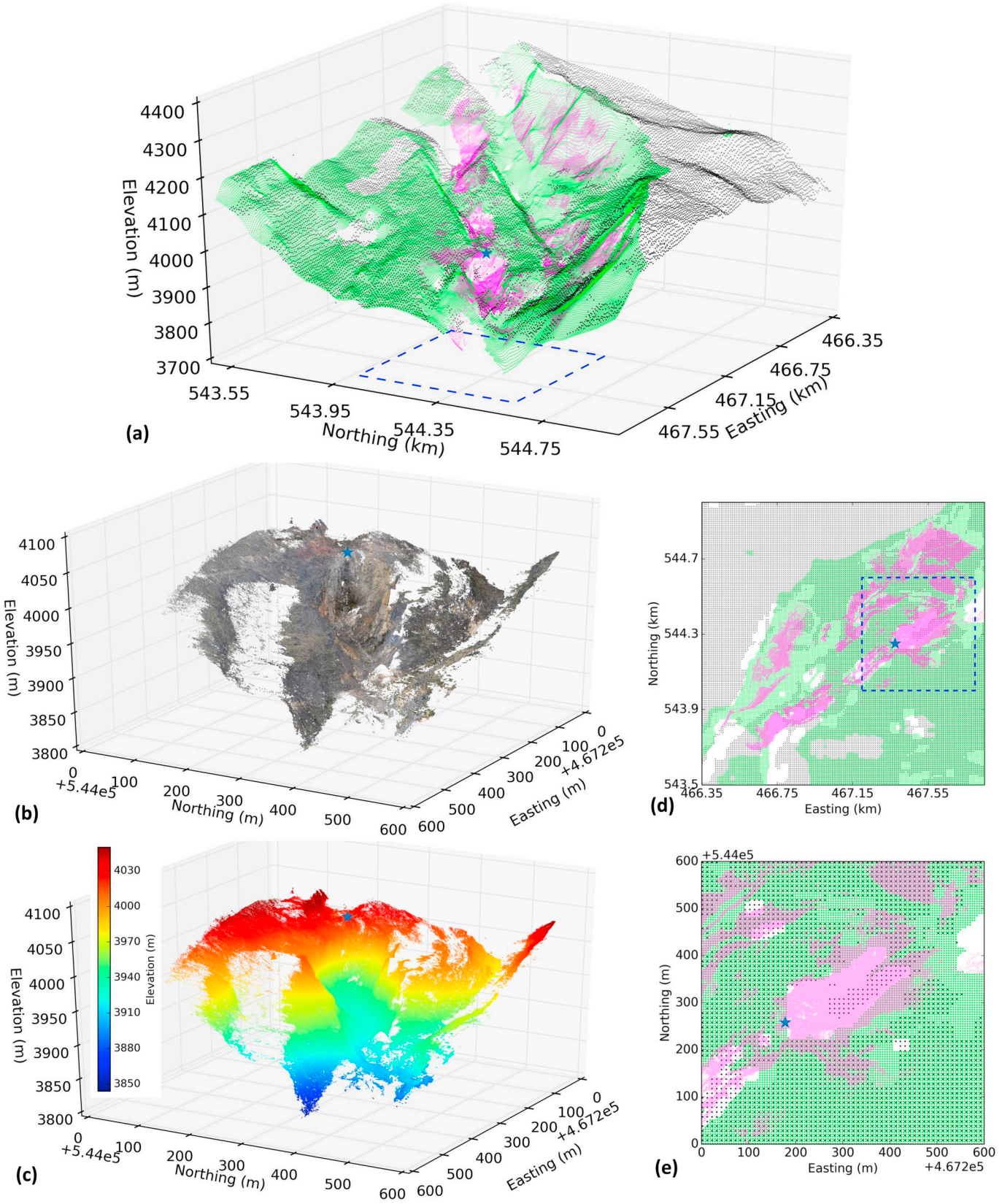

Fig. 7. (a) 3-D point cloud view of the TDX (black dots), TRI (green dots) and SfM (purple dots) DEMs at the upper part of the Azufrado channel. The blue box on the horizontal plane indicates the extent of (b), (c) and (e). (b) and (c) are the zoomed-in view of the SfM point cloud colored with photographic textures (Video S1) and elevation values, respectively. (d) is the 2-D view of (a). (e) is the 2-D zoomed-in view of the blue box in (a) and (d). The head of the waterfall is indicated by blue stars for reference.

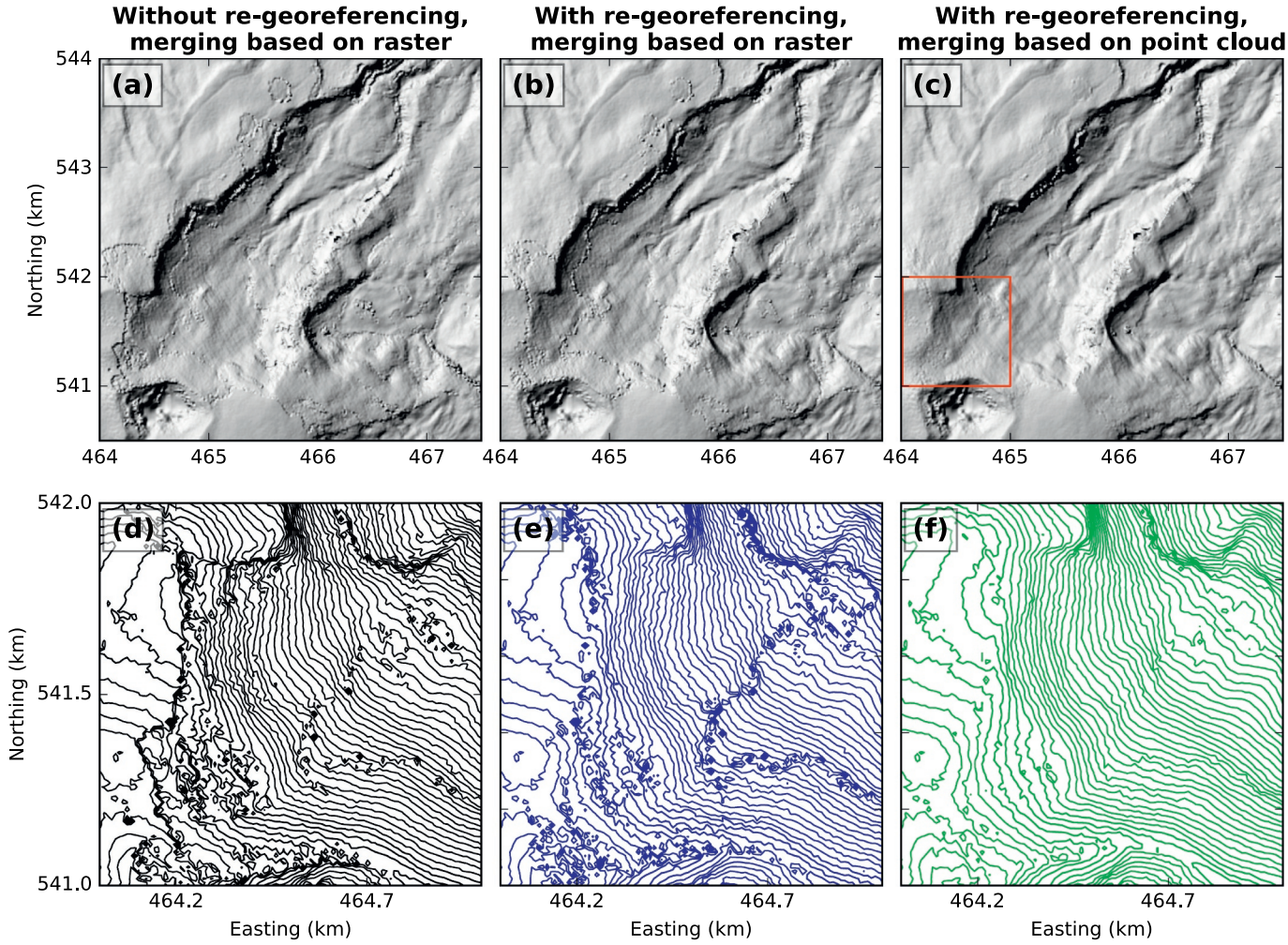

Fig. 8. Hillshade (top) and contour (bottom) maps of fused 10-m DEMs (TDX + TRI + SfM + SRTM) using different strategies. The weights used for the TDX, TRI, SfM and SRTM DEMs are 1, 2, 3, 1 for all the three fusion processes. For a certain point/pixel, the SRTM DEM is only used when other three data sets are not available. The northeastern part of the volcano is shown here as an example. (a) and (b) are based on the raster format without and with re-georeferencing the TRI and SfM DEMs. (c) is based on point clouds with the re-georeferencing process applied. The red box indicates the extent of (d), (e) and (f), which correspond to (a), (b) and (c) respectively. All contour maps have the same interval of 10 m. (For interpretation of the references to colour in this figure legend, the reader is referred to the web version of this article.)

The (non-uniform) spacing of the generated point cloud (Fig. 7b, c) is better than 10 cm in most areas. For the purposes of this research and to increase the data processing speed, the point cloud was sub-sampled with a minimum spacing of 1 m using CloudCompare, reducing the point cloud from ~20 million points to ~0.3 million points. As with the TRI data set, further geo-referencing is needed when merging the SfM point cloud into the TDX DEM.

3. Fusion of TDX, TRI, SfM and SRTM DEMs

Since the generated DEMs are in the same coordinate system, a simple and direct fusion algorithm would be to 1) re-sample the TRI and SfM DEMs to the same spatial spacing as the base DEM (TDX DEM); then 2) (weighted) average all available elevation values for a certain pixel based on raster format. This approach is used frequently and works surprisingly well in practice (e.g., Schultz et al., 1999; Schindler et al., 2011; Hoffmann et al., 2016; filling the gaps in the 30-m SRTM DEM with the 30-m AW3D in this research (Fig. 2a, b, Fig. 13b, c, d); Fig. S5). However, sometimes even a few meters elevation difference will result in rough edges at the interfaces of different data sets (Fig. 8a, b, d, e). For volcanic flow modeling, such artefacts may result in incorrect flow paths. The key problem of fusing DEMs generated from different data sources is the 3-D discrepancy (horizontal and vertical shifts) between DEMs. To reduce this discrepancy, we re-georeferenced the TRI and SfM DEMs to the TDX DEM, then used weighted averaging with multiple search distances based on point clouds to smooth data edges.

3.1. Re-georeferencing of the TRI and SfM DEMs

The TDX DEMs were geo-referenced to the SRTM DEM at about 1.5-pixel (10 × 10 m/pixel) horizontal accuracy (Table 2). The TRI and SfM DEMs were preliminarily geo-referenced based on GPS measurements, which are not evenly distributed. Since the TDX DEM has a much larger extent than the TRI and SfM DEMs, and has relatively high horizontal accuracy, the TDX DEM is used as the reference for correcting the TRI and SfM DEMs before the merging process.

The preliminarily geo-referenced TRI and SfMs DEMs have high precision, but do not have high accuracy. The relative position and elevation difference between a pixel/point and adjacent pixels/points are well represented by the TRI and SfM DEMs, however, the absolute position and elevation value may differ from the “true” value. In general, DEMs generated from different data sources with relatively high precision can be re-georeferenced to the reference DEM using a 3-D

Table 2
Average coherence of each TDX data pair, mean and standard deviation of elevation difference, and registration accuracy (Text S2, GAMMA Remote Sensing AG, 2014) between each TDX DEM and SRTM DEM.

Acquisition date (year-month-day)	Average coherence	Elevation difference between TDX DEM and SRTM DEM (m)		Registration accuracy between the TDX DEM and SRTM DEM (10 × 10 m/pixel)	
		Mean	Standard deviation	Ground-range (pixel)	Azimuth (pixel)
2012-12-09	0.63	−1.66	15.37	2.3	1.4
2013-07-23	0.70	−2.04	10.15	0.7	1.1
2013-08-03	0.60	−2.28	16.71	0.9	1.1
2014-04-13	0.77	−2.23	11.88	0.5	0.9
2013-09-12	0.67	−1.29	14.02	1.2	1.2
2013-09-23	0.72	−0.99	9.19	1.1	0.9
2014-05-12	0.77	−1.17	9.11	1.6	1.0
Average	0.69	−1.56	11.62	1.2	1.1

affine transformation, including translation, rotation, scaling and shearing (12 parameters, Eq. S1). To simplify the processing, shearing was not considered, and a uniform scaling is applied for all directions (7 parameters, Eq. (1), modified after Kutoglu et al., 2002):

$$\begin{bmatrix} x' \\ y' \\ z' \end{bmatrix} = \begin{bmatrix} t_x \\ t_y \\ t_z \end{bmatrix} + (1+s)\begin{bmatrix} 1 & \varepsilon_z & -\varepsilon_y \\ -\varepsilon_z & 1 & \varepsilon_x \\ \varepsilon_y & -\varepsilon_x & 1 \end{bmatrix}\begin{bmatrix} x \\ y \\ z \end{bmatrix} \quad (1)$$

where t_x, t_y and t_z are translation parameters along the three axes of right handed Cartesian coordinate system; ε_x, ε_y and ε_z are rotation parameters; s is the scale parameter; (x,y,z) and (x',y',z') are, in our case, the easting, northing and elevation of a certain point before and after re-georeferencing.

The re-georeferencing is performed based on 3-D point clouds. The SfM DEM is already in point cloud format with ~1-m spacing. The TDX and TRI DEMs which were originally in regular raster format were converted to 3-D point clouds (Fig. 7a) with 10-m and 5-m uniform horizontal spacing, respectively. Three independent point clouds were generated for the TRI DEMs obtained from the three TRI locations (Fig. 1b and Fig. 5). Considering the large differences in spacing and data coverage between the TDX, TRI and SfM point clouds, we registered the three TRI point clouds to TDX point cloud separately, then registered the SfM point cloud to the registered TRI point cloud. The 3-D point cloud registration was accomplished using the iterative closest point (ICP) algorithm (Besl and McKay, 1992) in the CloudCompare software. The ICP algorithm is classic and widely used for 3-D point cloud registration, e.g., 3-D LiDAR (Light Detection and Ranging) point cloud registration (e.g, Rusu and Cousins, 2011; Gressin et al., 2013). It is novel to apply it here to register multiple DEM products generated from different data sets with significantly different resolutions.

The elevation difference between the TRI and TDX DEM is > 10 meters in several areas before the re-georeferencing process (Fig. 9a-c). This was significantly reduced after processing (Fig. 9d-f, Fig. S6). The elevation difference between the SfM and TRI (re-georeferenced) DEMs was also significantly reduced by this re-georeferencing process (Fig. 10, Fig. S7). Remaining discrepancies between these DEMs may be due to the different original resolutions, errors in each DEM generation process, minor elevation changes due to different data acquisition time, or due to an over-simplified re-georeferencing process (nonuniform scaling and deformation, i.e., shearing, could be considered in the re-georeferencing process for higher accuracy).

Table 4
Simulated lahar run-out length using the 30-m SRTM DEM and the new 10-m DEM. Different lahar volumes are tested for both the Azufrado (Fig. S10) and Lagunillas channels while other parameters remain the same.

Channel name		Azufrado			Lagunillas		
Lahar volume ($\times 10^6$ m^3)		3.0	4.0	5.0	3.0	4.0	5.0
Run-out length (km)	30-m SRTM	29.4	34.7	38.5	30.3	34.3	39.9
	10-m new DEM	34.6	40.1	44.3	33.6	39.0	42.4
	Difference	5.2	5.4	5.8	3.3	4.7	2.5

3.2. Merging of TDX, TRI, SfM and SRTM DEMs

After the TRI and SfM DEMs were re-georeferenced to the TDX DEM, merging them directly based on raster format using the method mentioned at the beginning of this section results in elevation errors at the edges between the different data sets (Fig. 8b, e). To solve this problem, the merging process was performed based on a point cloud procedure using multiple (two in our case) search distances. Fig. 11 is a conceptual model of the merging process, which is a grid consisting of regular square cells of 10-m by 10-m spacing. The 30-m SRTM DEM with raster format was re-sampled to 10 m using bi-cubic interpolation in GDAL (Warmerdam, 2008), and converted to point cloud format. The elevation value at the center of each cell was calculated based on an adaptive method (see below) using the point clouds generated from four different data sets.

For a certain cell, distance from an elevation point to the cell center is used as the criterion to decide whether the point will be considered for elevation calculation or not. A circle with diameter D_1 centered at the cell center is used first as the search distance threshold. If at least one point from TDX, TRI or SfM falls in or on the circle (for instance, triangle 1 in Fig. 11), the elevation value of this cell will be the weighted average of all the points (not including the SRTM DEM) in and on the circle. If SRTM DEM is the only data source for the points falling in or on the circle (for instance, triangle 2 in Fig. 12), the circle diameter (i.e., search distance) is increased to D_2. The same processing will be applied to this new circle, but the SRTM points will be considered this time. In this case, if still no point from TDX, TRI or SfM falls in or on the circle, the elevation value of the nearest SRTM point will be used for this cell or the search distance may be increased again. Fig. 12 is a detailed flow chart of the above process for a certain grid cell. In our case we used two search distances with D_1 = 10 m and D_2 = 20 m (Fig. S8). For other applications, we suggest D_1 is the spatial resolution of the base DEM (10-m TDX DEM in our case), D_j is twice of D_{j-1} (j = 2, 3, …).

To reduce elevation discrepancies between DEMs generated from different data sets, a weighted averaging method is applied. Due to different spacing of TDX, TRI and SfM point clouds, many more SfM

Table 3
Comparison between three handheld GPS measurements and SfM DEM. The locations of these measurements are marked as yellow dots in Fig. 6a.

Handheld GPS measurement (m)			SfM DEM (m)			Difference between GPS & SfM DEM (m)		
Easting	Northing	Ellipsoidal height	Easting	Northing	Ellipsoidal height	Easting	Northing	Ellipsoidal height
467,207.6	544,159.2	4027.6	467,222.9	544,135.8	4028.9	15.3	−23.4	0.3
467,344.7	544,259.8	4005.6	467,359.8	544,243.0	4025.8	15.1	−16.8	20.3
467,436.5	544,225.0	4008.7	467,457.9	544,208.6	4025.9	21.4	−16.4	17.2
Average (m)						17.3	−18.9	12.6

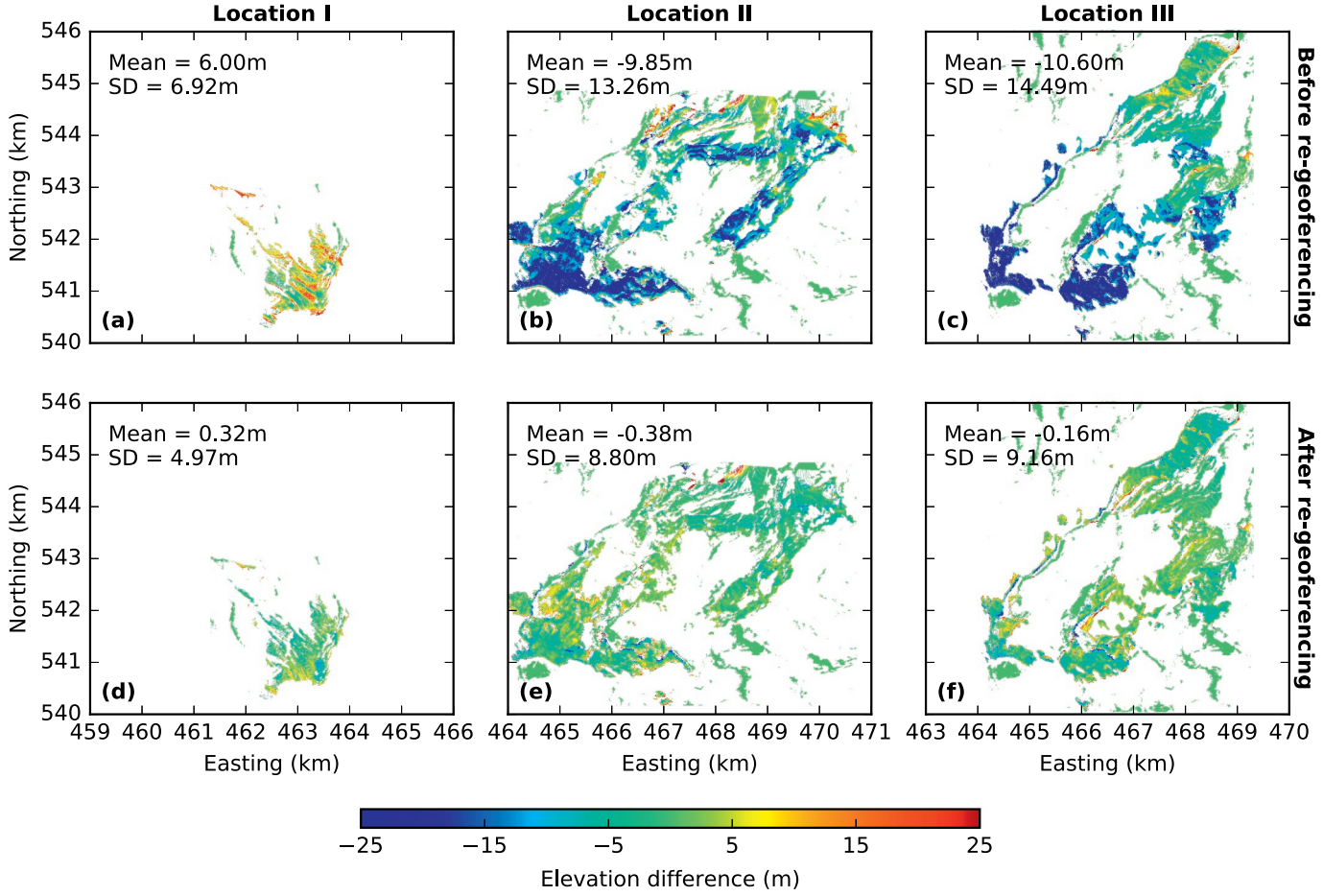

Fig. 9. Elevation difference between TDX and TRI DEMs before (top) and after (bottom) re-georeferencing the TRI DEMs. The TRI DEMs obtained at three different locations (Fig. 1b, Fig. 5) were re-georeferenced separately. Mean and SD values of each elevation difference map are labeled.

points may satisfy the search distance criteria compared to the TDX and TRI points for a certain grid cell. To avoid the elevation value of a cell being defined by the dominant data source, we calculate the average elevation of satisfying points for each data source first. Then different weights are assigned to the average elevation of each DEM to calculate a weighted average elevation as the final elevation value (Fig. 12). Higher weight is given to the data source with higher spatial resolution. In this study, we tested different weight values for TDX, TRI, SfM and SRTM DEMs (Fig. S9). We found that weight values of 1, 2, 3 and 1 respectively generated a DEM with relatively smooth elevation transition at edges of different data sets (Fig. 8c, f). If a certain data set does not have any point satisfying the search distance criterion, its weight will be 0 for that grid cell.

A DEM with 10-m resolution based on the above algorithm was

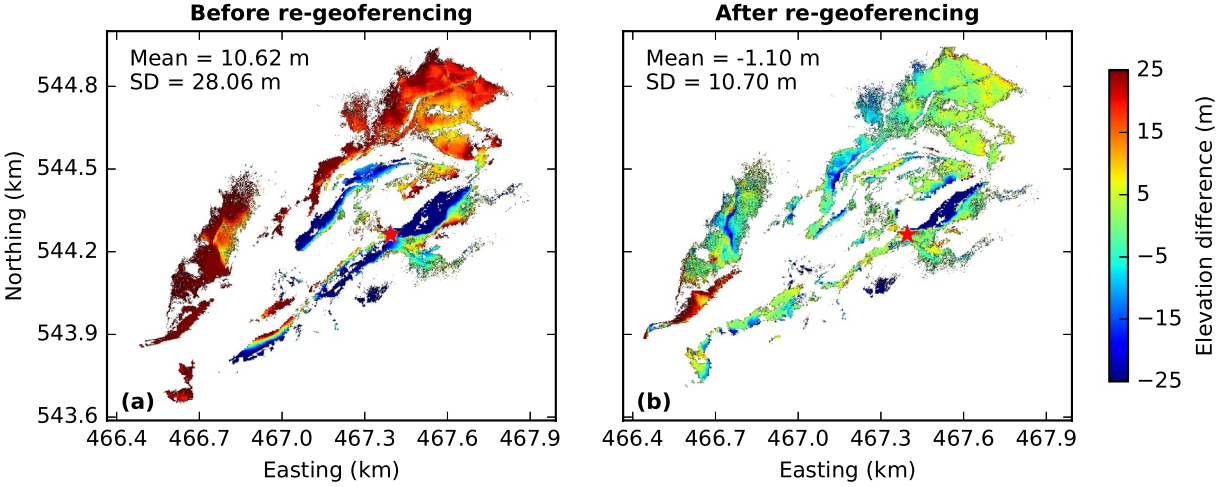

Fig. 10. (a) and (b) are maps of elevation difference between the SfM and re-georeferenced TRI DEMs before and after re-georeferencing the SfM DEM, respectively. The head of the waterfall is indicated by red stars for reference. Mean and SD values are labeled.

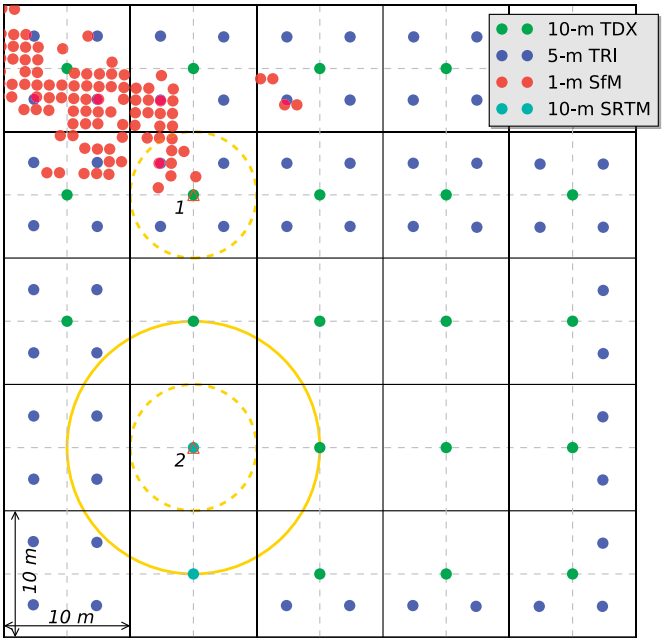

Fig. 11. Conceptual model for merging the 10-m TDX (green dots), 5-m TRI (blue dots), ~1-m SfM (red dots), and re-sampled 10-m SRTM (cyan dots) point clouds. The yellow dashed and solid circles represent the search distance criterions with diameters D_1 and D_2 ($D_2 > D_1$), respectively. Black hollow triangles indicate the center of two grid cells. (For interpretation of the references to colour in this figure legend, the reader is referred to the web version of this article.)

generated (Fig. 13a). TRI and SfM DEMs greatly reduced the data gaps in the TDX DEM in the northeastern part of the volcano (Fig. 13n, o, p). Zoomed-in hillshade maps (Fig. 13b-s) indicate significant improvement in the new DEM compared with the 30-m SRTM DEM representing more details of the rugged terrain. The hillshade map of the new 10-m DEM has a rougher texture than that of the 30-m SRTM DEM. Some features (e.g., small gullies) which are quite faint or not visible in the 30-m DEM, are revealed in the new 10-m DEM.

4. Modeling of volcanic mass flows

An accurate DEM is critical for the simulation of volcanic mass flows, such as lava flows, pyroclastic flows and lahars. Here we apply the new 10-m DEM and 30-m SRTM to 1) model lahar inundation zones with LaharZ, and 2) simulate the flow path, run out and thickness of pyroclastic flows using VolcFlow, to evaluate how much the new 10-m DEM affects volcanic flow hazard assessment. We apply the lahar model to a ~40-km section of the Lagunillas River, from the source to the junction with the Azufrado channel (Fig. 14), and we apply the pyroclastic flow model to the upper ~5 km of the Azufrado channel (Fig. 15). Both case studies are used here for evaluation purposes and do not reflect any particular past event at Nevado del Ruiz volcano. However, some data from the 1985 eruptive events (Pierson et al., 1990) are taken as references to better evaluate simulation results.

4.1. Simulation of lahar inundation zone in the Lagunillas channel

We applied the widely used USGS (United States Geological Survey) LaharZ model (Iverson et al., 1998; Schilling, 1998; Schilling, 2014) to simulate the lahar inundation zone. The model input parameters include a DEM, the drainage channel starting location, and a lahar

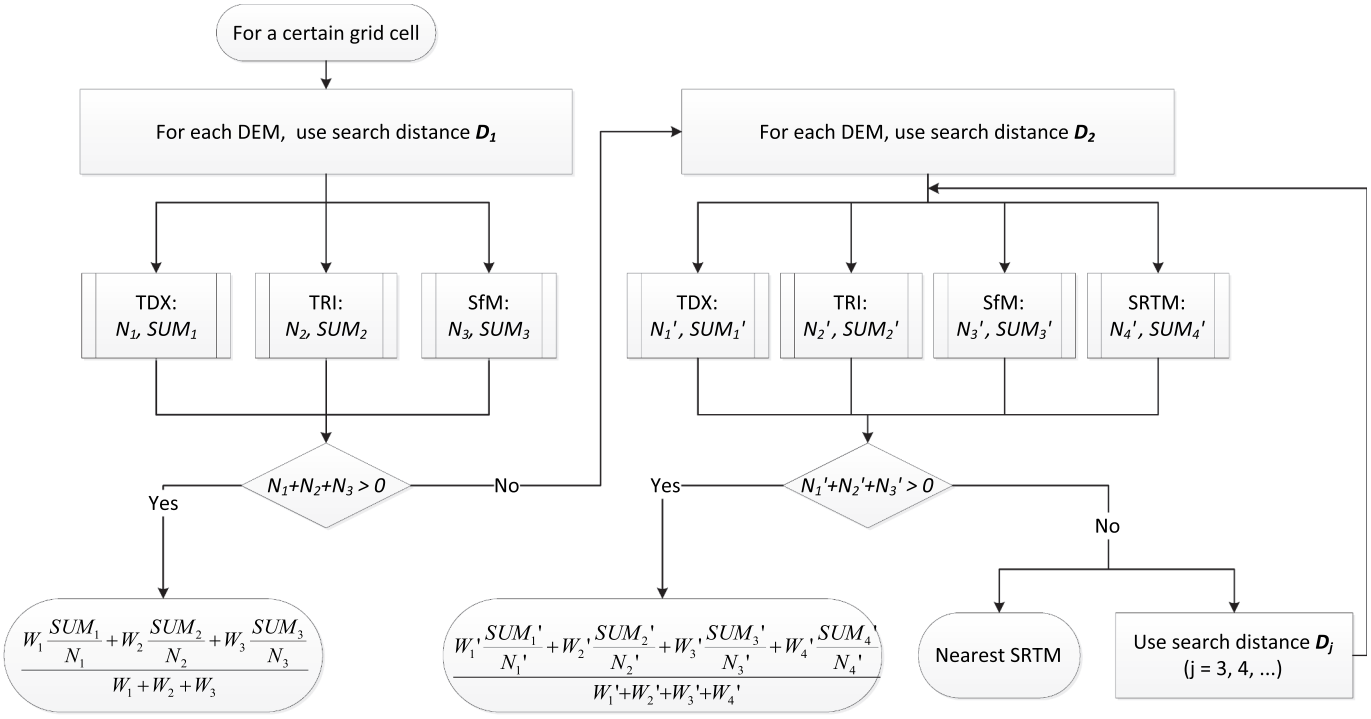

Fig. 12. Flow chart for merging the TDX, TRI, SfM and SRTM point clouds at a certain grid cell (Fig. 11). N_i and N_i' are, for each data source, the number of points falling in and on circles with D_1 and D_2 diameters, respectively. The subscript i equals 1, 2, 3 and 4, corresponding to TDX, TRI, SfM and SRTM, respectively. The same meaning for i is used in other parameters. SUM_i and SUM_i' are the sum of elevation values of the above satisfying points for each data source. W_i and W_i' are the weight of each data source when calculating the weighted-average elevation without and with the SRTM DEM, respectively. D_j ($j = 1, 2, 3, \ldots$) is the search distance (circle diameter). In this study, $W_1 = 1$, $W_2 = 2$, and $W_3 = 3$ ($W_1' = 1$, $W_2' = 2$, $W_3' = 3$, and $W_4' = 1$). Note that W_i or W_i' is 0 when the corresponding N_i or N_i' is 0.

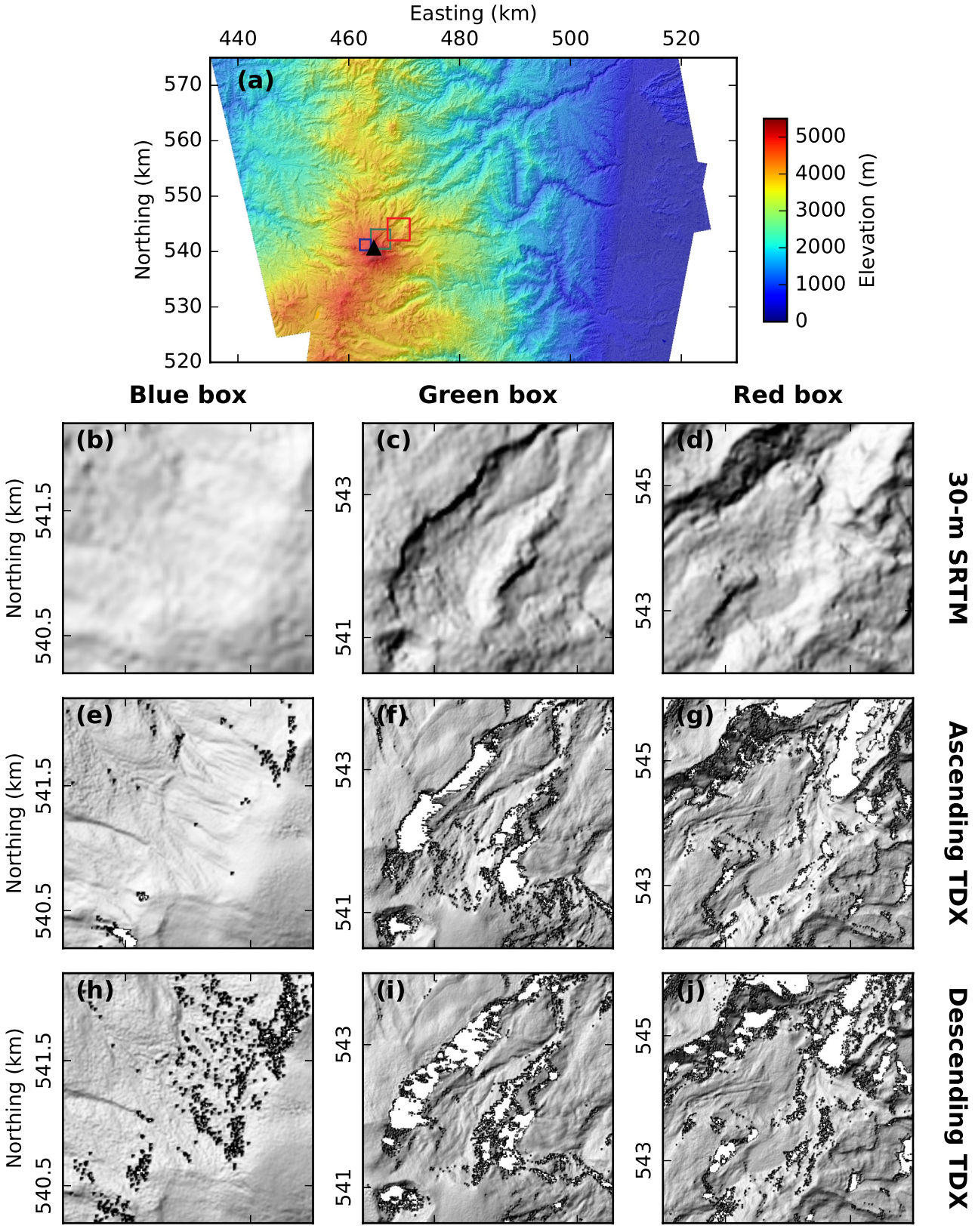

Fig. 13. (a) Elevation map of the new 10-m DEM generated by merging TDX, TRI, SfM and SRTM DEMs. The blue, green and red boxes show the extents of the zoomed-in hillshade maps in (b) - (s). The black triangle indicates the crater of the Nevado del Ruiz volcano. In (b) - (s), each column has the same extent. Rows correspond to the 30-m SRTM DEM, ascending (2012-12-09) TDX DEM, descending (2013-09-12) TDX DEM, TDX DEM combining all ascending and descending DEMs, merged DEM combining TDX, TRI and SfM DEMs, and the final 10-m DEM without data gaps. (For interpretation of the references to colour in this figure legend, the reader is referred to the web version of this article.)

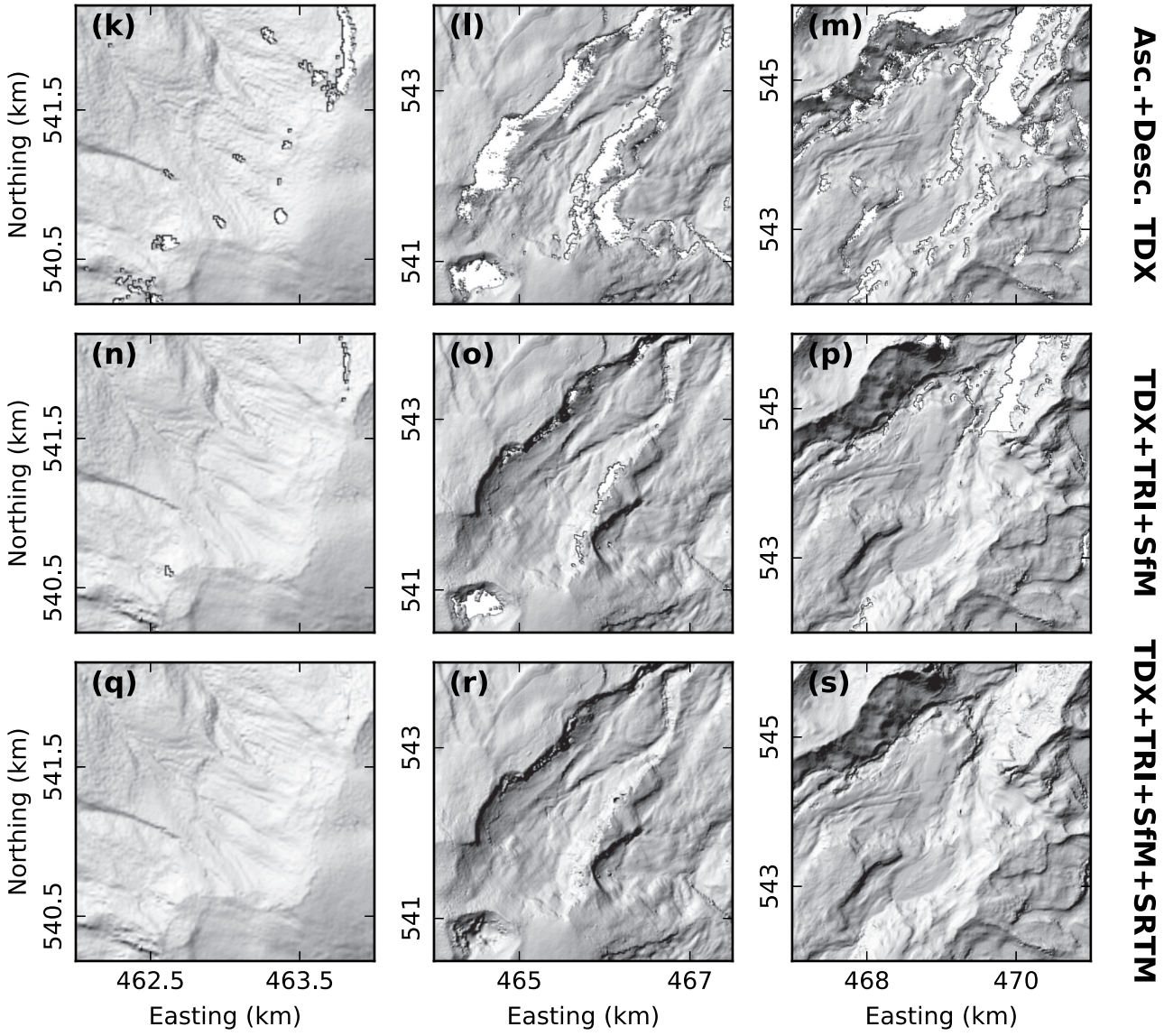

Fig. 13. (*continued*)

volume. The 30-m SRTM DEM and our new 10-m DEM were used for comparison. The same starting location (easting 467,914 m, northing 540,014 m) and lahar volume (4×10^6 m^3) were applied for these two DEMs. The input lahar volume is similar to the volume of lahars (~ 4×10^6–5×10^6 m^3) conveyed by the Lagunillas channel in 1985 in the area upstream to the junction with the Azufrado channel (Pierson et al., 1990).

The flow paths of simulated lahars using both DEMs are similar. The run out obtained using the new 10-m DEM is ~5 km longer (Fig. 14, Table 4). Simulated lahars using the 30-m SRTM DEMs stop just before the junction of the Azufrado and Lagunillas channels. However, the simulated lahars using the new 10-m DEM reaches and passes the junction (Fig. 14), which was observed during the 1985 lahars (Pierson et al., 1990). In our model, a larger lahar volume (5×10^6 m^3) is needed for the 30-m SRTM DEM to reach the same run-out distance as the new 10-m DEM (Table 4).

4.2. Simulation of pyroclastic flows in the upper Azufrado channel

The vigorous interaction between pyroclastic flows and the snow and ice on the summit of the Nevado del Ruiz volcano generated a great amount of melt water, which was the main contributor to the 1985 lahars (Pierson et al., 1990). Thick deposits of pyroclastic flows in the proximal area can also change topography and surface structure, which may affect the probability and magnitude of subsequent hazards, e.g., landslide, rock fall, debris flow, etc., and are often the cause of secondary lahars (i.e. lahars generated without any associated eruptive activity).

The VolcFlow numerical model (Kelfoun and Druitt, 2005; Kelfoun and Vargas, 2016) was applied to simulate the flow path, run out and thickness of pyroclastic flows in the upper Azufrado channel using the 30-m SRTM DEM and our new 10-m DEM. The same input parameters were used for both DEMs. Total initial volume (2×10^6 m^3) has the same order of magnitude as the reference total volume of the 1985 pyroclastic flows (9×10^6 m^3). Note that the latter represents the cumulative estimated volume from several flow events (Calvache, 1990). A mean density of 1500 kg/m^3 is used for pyroclastic flows, considering that the 1985 pyroclastic flows were rich in lithics (Pierson et al., 1990; Barberi et al., 1990). The constant retarding stress (here referred as 'Cohesion', 7500 Pa) and collisional stress coefficient (0.01) are set to the same values as the best-fit parameters used by Charbonnier and Gertisser (2012) in their VolcFlow modeling of the 2006 block-and-ash flows of Merapi Volcano, Indonesia. Travel time (1000 s) is set to be long enough compared to the source duration (100 s) to make sure that

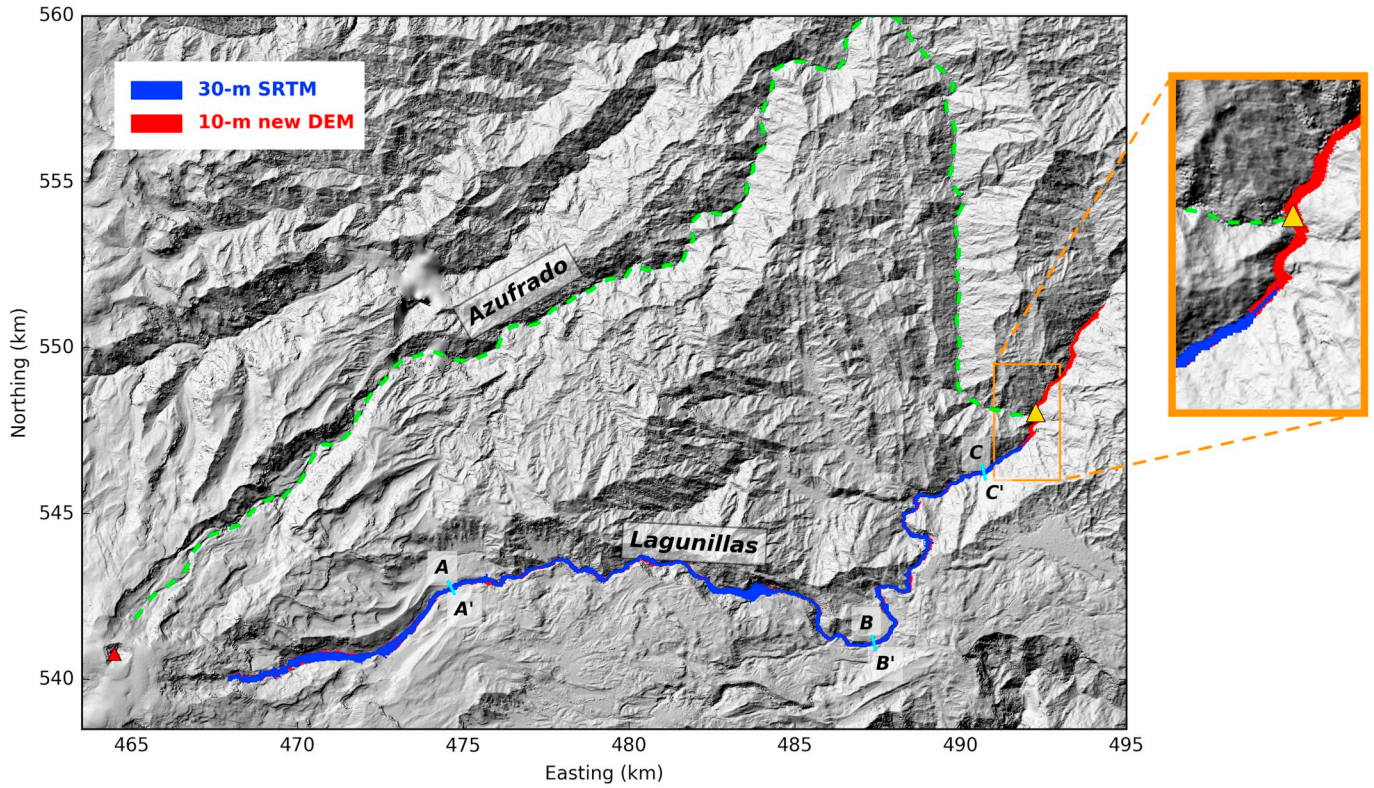

Fig. 14. Simulated inundation zones of Lahars in the Lagunillas channel based on the 30-m SRTM DEM (blue) and the new 10-m DEM (red). Note the overlay of the blue on the red. Yellow triangle indicates the junction location of the Azufrado (dashed green line) and Lagunillas channels. Red triangle indicates the crater of the Nevado del Ruiz volcano. Orange box is the zoomed-in view of the junction area. Cyan lines *AA′*, *BB′* and *CC′* show the locations of profiles in Fig. 17a, b and c. (For interpretation of the references to colour in this figure legend, the reader is referred to the web version of this article.)

the maximum flow velocity converges (Charbonnier and Gertisser, 2012).

Simulated pyroclastic flows based on both DEMs have almost the same flow paths (Fig. 15a, b, c). The run-out distance based on the new 10-m DEM is slightly shorter (Fig. 15a). The flow thicknesses using both DEMs have similar patterns (thinning near the crater, thickening in the channel center), however they exhibit more variation in areas with steep slopes. For example, at the waterfall area of the Azufrado channel, the valley walls are nearly vertical with an elevation change of approximately 70 m (Fig. 7b, Fig. 15d). The simulated pyroclastic flows using the new 10-m DEM are well constrained in the valley bottom (Fig. 15f). However, the simulated pyroclastic flows using the 30-m SRTM DEM spread laterally beyond the valley walls (which is unlikely in reality), and the thickness and extent of the pyroclastic deposit are poorly constrained by the changes in channel geometries (Fig. 15e).

In general, the simulated pyroclastic flow using the 30-m SRTM DEM has a larger extent of relatively thin (< 6 m in our case) deposits (Fig. 16a) while the new 10-m DEM has a larger extent of relatively thick (≥ 6 m) deposits (Fig. 16b).

5. Discussion

Geomorphic analysis is used to evaluate the effects of different digital channel representations for the simulations of volcanic mass flows at Nevado del Ruiz volcano. In general, deeply cut valleys and channels are deeper in our new 10-m DEM than those in the 30-m SRTM DEM (Fig. 17a-f). Sections of the Lagunillas and Azufrado channels with V-shape geometries are poorly reproduced in the 30-m SRTM DEM with a shallower and flatter floor (Fig. 17a, b, d, e) compared to the 10-m DEM. Similarly, sections of the channels with U-shape geometries (Fig. 17c, f) are better reproduced in the 10-m DEM with a flatter and deeper floor than those of the 30-m SRTM DEM. In most cases low spatial resolution of a DEM has a smoothing effect on topography. However, in some situations (e.g., Fig. 17f), it may result in steeper elevation changes. Other factors, e.g., sensor type and looking angle, may also affect the representation of channel features in the final DEM.

The equations used in LaharZ to relate lahar volume V to a cross-section inundation area A (Fig. 17c), and a planimetric inundation area B are (Schilling, 2014):

$$A = 0.05V^{2/3} \quad (2)$$

$$B = 200V^{2/3} \quad (3)$$

When lahar volume V (4×10^6 m^3) is the same for the 30-m SRTM DEM and the new 10-m DEM, the calculated cross-section inundation area A (1260 m^2), and the simulated planimetric inundation area B (5.0 km^2) are also the same for both DEMs based on Eqs. (2) and (3). Simulated planimetric inundation area B can also be expressed as:

$$B = \int_0^L C_L dx \quad (4)$$

where L is the total length of the simulated lahar inundation zone, and C_L is the cross-section inundation length (Fig. 17c). For a certain lahar volume V, when C_L decreases, L will increase based on Eqs. (3) and (4). For steep-slope valleys and channels, to achieve the same cross-section inundation area A, C_L is usually shorter using the new 10-m DEM compared to the 30-m SRTM DEM (Fig. 17a, b, c). This difference causes the simulated lahar inundation zone using the 10-m DEM to have a longer run-out distance L (Fig. 14, S10, Table 4). According to Eq. (4), if L is the same using the above two DEMs, the 30-m SRTM DEM will yield a larger B value. Based on Eq. (3) $B = 200V^{2/3}$, the lahar volume V will need to be larger.

For the pyroclastic flow simulation using VolcFlow, the deposit thickness corresponds positively to channel-wall slopes. Simulated flows are more constrained (thicker deposit) when the channel floor is

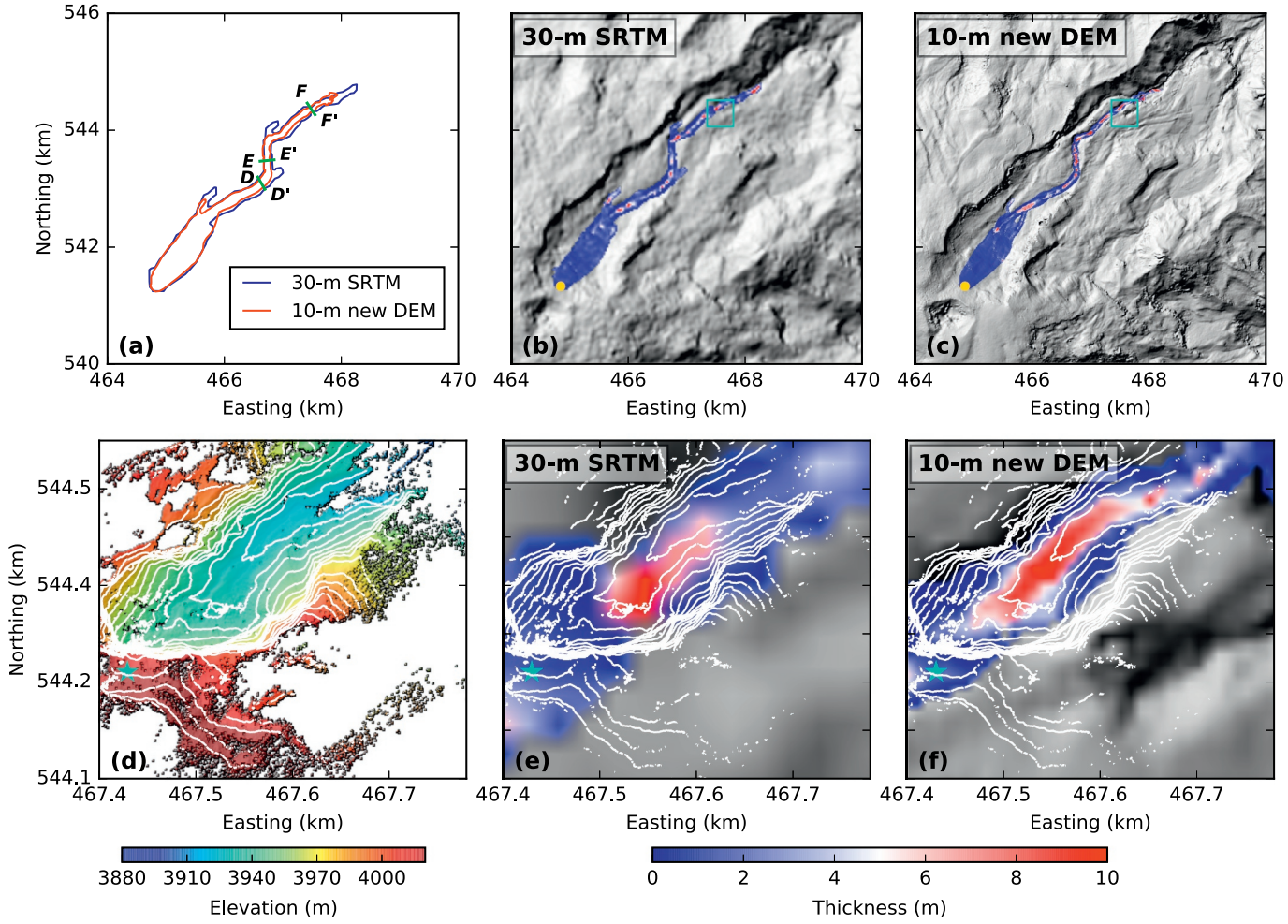

Fig. 15. Simulated pyroclastic flows based on the 30-m SRTM and our new 10-m DEMs. (a) Run out of the simulated pyroclastic flows. Green lines *DD′*, *EE′* and *FF′* show the locations of profiles in Fig. 17d, e and f. (b) and (c) are flow thickness maps. Yellow dots indicate the starting location of the flows. Cyan boxes indicate the extent of (d), (e) and (f), which are the zoomed-in view of the waterfall area of the Azufrado channel. (d) Elevation map of the waterfall area generated from the ~1-m SfM DEM. White lines are elevation contours with an interval of 6 m. Dense contour lines indicate steep slopes. (e) and (f) are the zoomed-in view of the pyroclastic flows at the waterfall area. The head of the waterfall is indicated by cyan stars for reference. White lines are the same elevation contours as (d). (For interpretation of the references to colour in this figure legend, the reader is referred to the web version of this article.)

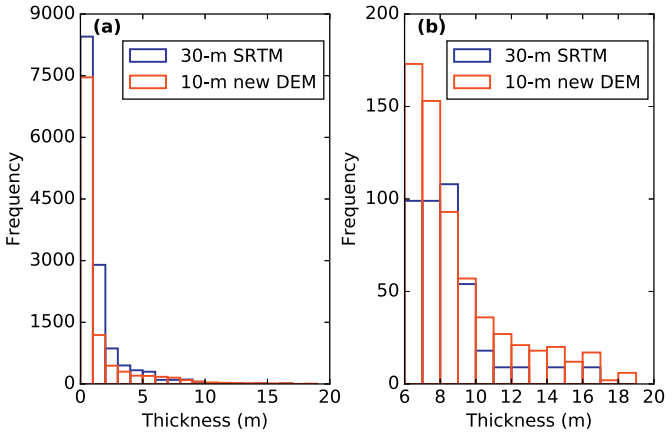

Fig. 16. Histograms of thickness maps of the simulated pyroclastic flows using the 30-m SRTM DEM (blue) and our new 10-m DEM (red). The frequency of the 30-m SRTM DEM was adjusted (multiplied by 9) considering the three-times resolution difference (corresponding to nine-times area difference). (b) is a zoomed-in view of (a) with thickness > 6 m. (For interpretation of the references to colour in this figure legend, the reader is referred to the web version of this article.)

narrow (V-shape) and spread out (thinner deposit) when the channel floor is wide (U-shape) (Fig. 17d, e, f). The general smoothing effect of the 30-m SRTM DEM causes the simulated pyroclastic flow to have a smaller extent of thick deposit compared to the 10-m DEM (Fig. 16b).

6. Conclusions

To our knowledge, this is the first study combining satellite radar, ground based radar, ground-based photography, and freely available global DEMs to generate a high-resolution DEM without data gaps. TDX data show their remarkable ability to generate high-resolution and high-accuracy DEMs at regional scales. Ground based TRI and SfM data greatly reduced the data gaps in the TDX DEM for Nevado del Ruiz volcano (Fig. 7a, d, e; Fig. 13n, o, p). 3-D point cloud matching using iterative closest point (ICP) algorithm is an effective and efficient way to automatically re-georeference DEMs with different resolutions. We developed an adaptive algorithm with multiple search distances to merge the point clouds from different data sources and different resolutions. Compared with merged DEMs using other methods, our DEM has smoother elevation transitions at data edges (Fig. 8). The DEM fusing process based on 3-D point clouds provides insights into fusing DEMs from multiple sensors with different resolutions.

Compared to our new 10-m DEM, the simulated run-out distance of

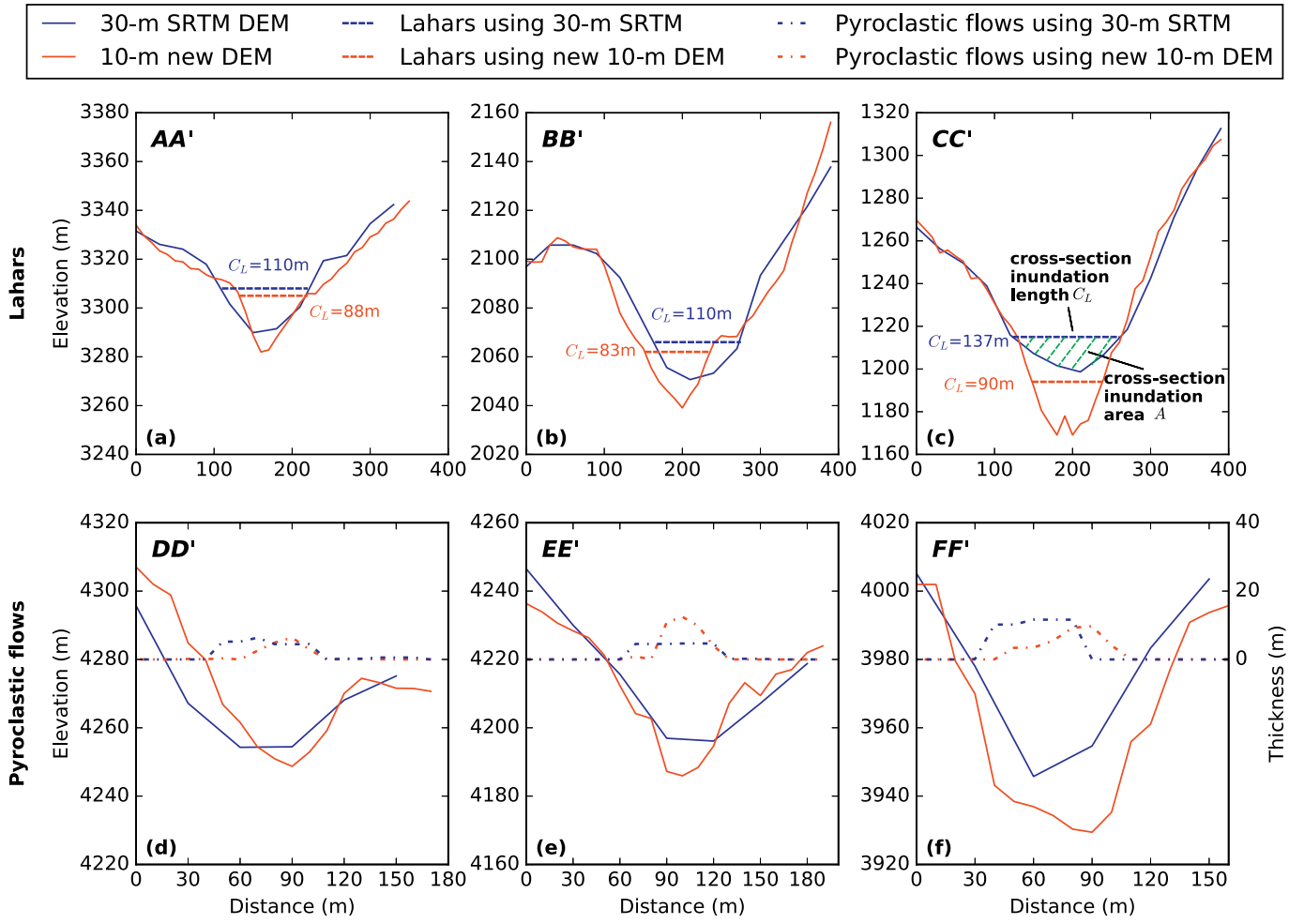

Fig. 17. Profiles of elevations (solid lines), simulated lahar inundation zones (dashed lines, top) and pyroclastic flow thicknesses (dashed dotted lines, bottom) based on the 30-m SRTM DEM (blue) and our new 10-m DEM (red). The values of the cross-section inundation length C_L are labeled. Locations of profiles are shown in Fig. 14 and 15a. (For interpretation of the references to colour in this figure legend, the reader is referred to the web version of this article.)

the lahar inundation zone and the extent of relatively thick deposits of pyroclastic flows are likely to be underestimated or unrealistic when using the 30-m SRTM DEM. Up-to-date DEMs with high resolution (~ 10 m or better) need to be generated for active volcanoes in or near densely populated areas (e.g., Colima volcano, Mexico; Fuego volcano, Guatemala; and Merapi and Sinabung volcanoes, Indonesia) to improve volcanic flow hazard assessment. The fastest response time can be one day when using a single data source (e.g., TRI or SfM) to generate DEM for erupting volcanoes for a relatively small area. This will increase to several days to weeks when satellite data and terrestrial data need to be combined to generate a DEM with higher quality and larger coverage.

High-resolution DEMs will not only improve mass flow modeling for active volcanoes, but can also be used to quantify morphological changes (e.g., runout, thickness and volume) due to the emplacement of new volcanic flow deposits by generating DEMs before and after volcanic activities (e.g., Wadge et al., 2011; Poland, 2014; Albino et al., 2015; Kubanek et al., 2015a, 2015b; Arnold et al., 2016; Bagnardi et al., 2016; Carr et al., 2018). Smaller-scale higher-resolution topography of critical areas, e.g., river channels, can be combined with larger-scale lower-resolution topography. This can reduce the need to collect high-resolution data for an entire survey area. More work is required to quantify how the resolution of elevation models affects model runtime, runout estimation and inundation area. Both high- and low-resolution DEMs can provide a useful tool for forecasting mass flow inundation based on flow volume (Kubanek et al., 2015a). The use of drones in data collection for SfM will be more widely used as technology improves. Future SfM studies can consider several data acquisitions over an extended period (to increase the chances of good weather) and a drone suitable for high altitude (> 4000 m) operation or kite photography.

Supplementary data to this article can be found online at https://doi.org/10.1016/j.rse.2019.111348.

Acknowledgments

We thank Charles Connor for initially suggesting the study, staff from the Colombian Geological Service and their field crew for invaluable assistance in the field, and David Pyle for suggestions and encouraging this integrated study. Julia Kubanek and three anonymous reviewers made a number of constructive comments which greatly improved the manuscript. We thank editors Jing M. Chen and Dar Roberts for their patience and guidance. We thank the USF Alliance for Integrative Spatial Technologies (AIST) for loan of a drone. We thank the German Aerospace Center (DLR) for providing TanDEM-X SAR data and the 90-m TDX DEM (https://geoservice.dlr.de/web/dataguide/tdm90/). Landsat-8 image and SRTM DEM were downloaded from the United States Geological Survey (USGS) Earth Explorer platform (http://earthexplorer.usgs.gov/). 30-m ALOS World 3D (AW3D30) was provided by the Japan Aerospace Exploration Agency (JAXA), and was downloaded from https://www.eorc.jaxa.jp/ALOS/en/aw3d30/index.htm. The ASTER DEM (Version 2) is downloaded from LP DAAC Global Data Explorer (https://gdex.cr.usgs.gov/gdex/). This study was supported by a National Science Foundation (NSF) RAPID grant, EAR

1546924, to Timothy Dixon and Sylvain Charbonnier. Partial field work support came from the UK Natural Environment Research Council (NERC) STREVA grant NE/J020001/1. Fanghui Deng was partially supported by NSF grant 1347899 and NASA Earth and Space Science Fellowship during this study. The new 10-m DEM is available at http://labs.cas.usf.edu/geodesy/ under the Data Sharing section.

References

Albino, F., Smets, B., d'Oreye, N., Kervyn, F., 2015. High-resolution TanDEM-X DEM: an accurate method to estimate lava flow volumes at Nyamulagira volcano (DR Congo). Journal of Geophysical Research: Solid Earth 120 (6), 4189–4207.

Arnold, D.W.D., Biggs, J., Wadge, G., Ebmeier, S.K., Odbert, H.M., Poland, M.P., 2016. Dome growth, collapse, and valley fill at Soufrière Hills volcano, Montserrat, from 1995 to 2013: contributions from satellite radar measurements of topographic change. Geosphere 12 (4), 1300–1315.

Arnold, D.W.D., Biggs, J., Anderson, K., Vallejo Vargas, S., Wadge, G., Ebmeier, S.K., Naranjo, M.F., Mothes, P., 2017. Decaying lava extrusion rate at El Reventador Volcano, Ecuador, measured using high-resolution satellite radar. Journal of Geophysical Research: Solid Earth 122 (12), 9966–9988.

Astronaut photograph ISS023-E-27737, 2010. https://eol.jsc.nasa.gov/SearchPhotos/photo.pl?mission=ISS023&roll=E&frame=27737.

Avtar, R., Yunus, A.P., Kraines, S., Yamamuro, M., 2015. Evaluation of DEM generation based on interferometric SAR using TanDEM-X data in Tokyo. Physics and Chemistry of the Earth, Parts A/B/C 83, 166–177.

Bagnardi, M., González, P.J., Hooper, A., 2016. High-resolution digital elevation model from tri-stereo Pleiades-1 satellite imagery for lava flow volume estimates at Fogo Volcano. Geophys. Res. Lett. 43 (12), 6267–6275.

Barberi, F., Martini, M., Rosi, M., 1990. Nevado del Ruiz volcano (Colombia): pre-eruption observations and the November 13, 1985 catastrophic event. J. Volcanol. Geotherm. Res. 42 (1–2), 1–12.

Besl, P.J. and McKay, N.D., 1992. Method for registration of 3-D shapes. In sensor fusion IV: control paradigms and data structures (Vol. 1611, pp. 586-607). International Society for Optics and Photonics.

Caduff, R., Schlunegger, F., Kos, A., Wiesmann, A., 2015. A review of terrestrial radar interferometry for measuring surface change in the geosciences. Earth Surf. Process. Landf. 40 (2), 208–228.

Calvache, M.L.V., 1990. Pyroclastic deposits of the November 13, 1985 eruption of Nevado del Ruiz volcano, Colombia. J. Volcanol. Geotherm. Res. 41 (1–4), 67–78.

Capra, L., Manea, V.C., Manea, M., Norini, G., 2011. The importance of digital elevation model resolution on granular flow simulations: a test case for Colima volcano using TITAN2D computational routine. Nat. Hazards 59 (2), 665–680.

Carr, B.B., Clarke, A.B., Arrowsmith, J.R., Vanderkluysen, L., Dhanu, B.E., 2018. The emplacement of the active lava flow at Sinabung Volcano, Sumatra, Indonesia, documented by structure-from-motion photogrammetry. J. Volcanol. Geotherm. Res. In Press. https://doi.org/10.1016/j.jvolgeores.2018.02.004.

Charbonnier, S.J., Gertisser, R., 2009. Numerical simulations of block-and-ash flows using the Titan2D flow model: examples from the 2006 eruption of Merapi Volcano, Java, Indonesia. Bull. Volcanol. 71 (8), 953–959.

Charbonnier, S.J., Gertisser, R., 2012. Evaluation of geophysical mass flow models using the 2006 block-and-ash flows of Merapi Volcano, Java, Indonesia: towards a short-term hazard assessment tool. J. Volcanol. Geotherm. Res. 231, 87–108.

Charbonnier, S.J., Deng, F., Dixon, T.H. and Malservisi, R., 2018, July. High-resolution Dems of active volcanoes from tandem-X data: implications for flow modeling and hazard assessment. In IGARSS 2018-2018 IEEE International Geoscience and Remote Sensing Symposium (pp. 399-402). IEEE.

CloudCompare (version 2.9), 2017. GPL software. http://www.cloudcompare.org.

CloudCompare user manual, 2015. version 2.6.1, on line at: http://www.danielgm.net/cc/doc/qCC/CloudCompare%20v2.6.1%20%20User%20manual.pdf.

Crosetto, M., 2002. Calibration and validation of SAR interferometry for DEM generation. ISPRS J. Photogramm. Remote Sens. 57 (3), 213–227.

Deo, R., Rossi, C., Eineder, M., Fritz, T., Rao, Y.S., & Lachaise, M., 2014. Fusion of ascending and descending pass raw TanDEM-X DEM. 2014 IEEE geoscience and remote sensing symposium (pp. 21-24). IEEE.

Deo, R., Rossi, C., Eineder, M., Fritz, T., Rao, Y.S., 2015. Framework for fusion of ascending and descending pass TanDEM-X raw DEMs. IEEE Journal of Selected Topics in Applied Earth Observations and Remote Sensing 8 (7), 3347–3355.

Dixon, T.H., Voytenko, D., Lembke, C., Peña, S., Howat, I., Gourmelen, N., Werner, C.L., Oddsson, B., 2012. Emerging technology monitors ice-sea interface at outlet glaciers. Eos, Transactions American Geophysical Union 93 (48), 497–498.

Ehsani, A.H., Quiel, F., 2008. Application of self organizing map and SRTM data to characterize yardangs in the Lut desert, Iran. Remote Sens. Environ. 112 (7), 3284–3294.

Eineder, M., 2003, December. Problems and solutions for InSAR digital elevation model generation of mountainous terrain. In Proc. Fringe 2003 Workshop, Frascati, Italy.

Eineder, M., Runge, H., Boerner, E., Bamler, R., Adam, N., Schättler, B., Breit, H. and Suchandt, S., 2003. SAR interferometry with TerraSAR-X. In Proc. of FRINGE 2003 Workshop, Frascati, Italy (Vol. 15).

Farr, T.G., Rosen, P.A., Caro, E., Crippen, R., Duren, R., Hensley, S., Kobrick, M., Paller, M., Rodriguez, E., Roth, L., Seal, D., 2007. The shuttle radar topography mission. Rev. Geophys. 45 (2).

Gamba, P., Dell'Acqua, F., Houshmand, B., 2003. Comparison and fusion of LIDAR and InSAR digital elevation models over urban areas. Int. J. Remote Sens. 24 (22), 4289–4300.

GAMMA Remote Sensing AG, 2008. Differential interferometry and geocoding software -DIFF&GEO, geocoding and image registration. User's guide, version 1.3, Gümligen, Switzerland.

GAMMA Remote Sensing AG, 2014. Interferometric SAR Processor - ISP. User's Guide, Version 1.8, Gümligen, Switzerland.

Gelautz, M., Paillou, P., Chen, C.W., Zebker, H.A., 2003. Radar stereo-and interferometry-derived digital elevation models: comparison and combination using Radarsat and ERS-2 imagery. Int. J. Remote Sens. 24 (24), 5243–5264.

Global Volcanism Program, 2013. Volcanoes of the World, v. 4.7.5. Venzke, E (ed.). Smithsonian Institution. https://volcano.si.edu/.

Global Volcanism Program, 2017. Report on Nevado del Ruiz (Colombia). In: Venzke, E. (Ed.), Bulletin of the Global Volcanism Network, 42:6, (Smithsonian Institution).

Gressin, A., Mallet, C., Demantké, J., David, N., 2013. Towards 3D lidar point cloud registration improvement using optimal neighborhood knowledge. ISPRS J. Photogramm. Remote Sens. 79, 240–251.

Hayakawa, E.H., Rossetti, D.F., Valeriano, M.M., 2010. Applying DEM-SRTM for reconstructing a late Quaternary paleodrainage in Amazonia. Earth Planet. Sci. Lett. 297 (1–2), 262–270.

Hirano, A., Welch, R., Lang, H., 2003. Mapping from ASTER stereo image data: DEM validation and accuracy assessment. ISPRS J. Photogramm. Remote Sens. 57 (5), 356–370.

Hirt, C., Filmer, M.S., Featherstone, W.E., 2010. Comparison and validation of the recent freely available ASTER-GDEM ver1, SRTM ver4. 1 and GEODATA DEM-9S ver3 digital elevation models over Australia. Aust. J. Earth Sci. 57 (3), 337–347.

Hoffmann, J., Huber, M., Marschalk, U., Wendleder, A., Wessel, B., Bachmann, M., Bräutigam, B., Busche, T., González, J.H., Krieger, G., Rizzoli, P., Eineder, M., Fritz, T., 2016. TanDEM-X ground segment DEM products specification document. Public document TD-GS-PS-0021, issue 3.1, DLR, Germany.

Hubbard, B.E., Sheridan, M.F., Carrasco-Núñez, G., Díaz-Castellón, R., Rodríguez, S.R., 2007. Comparative lahar hazard mapping at Volcano Citlaltépetl, Mexico using SRTM, ASTER and DTED-1 digital topographic data. J. Volcanol. Geotherm. Res. 160 (1), 99–124.

Huggel, C., Schneider, D., Miranda, P.J., Granados, H.D., Kääb, A., 2008. Evaluation of ASTER and SRTM DEM data for lahar modeling: a case study on lahars from Popocatépetl Volcano, Mexico. J. Volcanol. Geotherm. Res. 170 (1), 99–110.

Iverson, R.M., Schilling, S.P., Vallance, J.W., 1998. Objective delineation of lahar-inundation hazard zones. Geol. Soc. Am. Bull. 110 (8), 972–984.

James, M.R., Robson, S., 2012. Straightforward reconstruction of 3D surfaces and topography with a camera: accuracy and geoscience application. J. Geophys. Res. Earth Surf. 117, 1–17.

Jarihani, A.A., Callow, J.N., McVicar, T.R., Van Niel, T.G., Larsen, J.R., 2015. Satellite-derived digital elevation model (DEM) selection, preparation and correction for hydrodynamic modelling in large, low-gradient and data-sparse catchments. J. Hydrol. 524, 489–506.

Jiang, H., Zhang, L., Wang, Y., Liao, M., 2014. Fusion of high-resolution DEMs derived from COSMO-SkyMed and TerraSAR-X InSAR datasets. J. Geod. 88 (6), 587–599.

Kääb, A., 2005. Combination of SRTM3 and repeat ASTER data for deriving alpine glacier flow velocities in the Bhutan Himalaya. Remote Sens. Environ. 94 (4), 463–474.

Karkee, M., Steward, B.L., Aziz, S.A., 2008. Improving quality of public domain digital elevation models through data fusion. Biosyst. Eng. 101 (3), 293–305.

Kelfoun, K., Druitt, T.H., 2005. Numerical modeling of the emplacement of Socompa rock avalanche, Chile. Journal of Geophysical Research: Solid Earth 110 (B12).

Kelfoun, K., Vargas, S.V., 2016. VolcFlow capabilities and potential development for the simulation of lava flows. Geol. Soc. Lond., Spec. Publ. 426 (1), 337–343.

Kolzenburg, S., Favalli, M., Fornaciai, A., Isola, I., Harris, A.J.L., Nannipieri, L., Giordano, D., 2016. Rapid updating and improvement of airborne LIDAR DEMs through ground-based SfM 3-D modeling of volcanic features. IEEE Trans. Geosci. Remote Sens. 54 (11), 6687–6699.

Krieger, G., Moreira, A., Fiedler, H., Hajnsek, I., Werner, M., Younis, M., Zink, M., 2007. TanDEM-X: A satellite formation for high-resolution SAR interferometry. IEEE Trans. Geosci. Remote Sens. 45 (11), 3317–3341.

Kubanek, J., Richardson, J.A., Charbonnier, S.J., Connor, L.J., 2015a. Lava flow mapping and volume calculations for the 2012–2013 Tolbachik, Kamchatka, fissure eruption using bistatic TanDEM-X InSAR. Bull. Volcanol. 77 (12), 106.

Kubanek, J., Westerhaus, M., Schenk, A., Aisyah, N., Brotopuspito, K.S., Heck, B., 2015b. Volumetric change quantification of the 2010 Merapi eruption using TanDEM-X InSAR. Remote Sens. Environ. 164, 16–25.

Kubanek, J., Westerhaus, M., Heck, B., 2017. TanDEM-X time series analysis reveals lava flow volume and effusion rates of the 2012–2013 Tolbachik, Kamchatka fissure eruption. Journal of Geophysical Research: Solid Earth 122 (10), 7754–7774.

Kutoglu, H.S., Mekik, C., Akcin, H., 2002. A comparison of two well known models for 7-parameter transformation. Australian surveyor 47 (1), 24–30.

Lee, J.S., Jurkevich, L., Dewaele, P., Wambacq, P., Oosterlinck, A., 1994. Speckle filtering of synthetic aperture radar images: A review. Remote Sens. Rev. 8 (4), 313–340.

Londoño, J.M., 2016. Evidence of recent deep magmatic activity at Cerro Bravo-Cerro Machín volcanic complex, central Colombia. Implications for future volcanic activity at Nevado del Ruiz, Cerro Machín and other volcanoes. J. Volcanol. Geotherm. Res. 324, 156–168.

Lowe, D.R., Williams, S.N., Leigh, H., Connort, C.B., Gemmell, J.B., Stoiber, R.E., 1986. Lahars initiated by the 13 November 1985 eruption of Nevado del Ruiz, Colombia. Nature 324, 51–53.

Lu, Z., Mann, D., Freymueller, J.T., Meyer, D.J., 2000. Synthetic aperture radar interferometry of Okmok volcano, Alaska: radar observations. Journal of Geophysical Research: Solid Earth 105 (B5), 10791–10806.

Ludwig, R., Schneider, P., 2006. Validation of digital elevation models from SRTM X-SAR

for applications in hydrologic modeling. ISPRS J. Photogramm. Remote Sens. 60 (5), 339–358.
Lundgren, P., Samsonov, S.V., López Velez, C.M., Ordoñez, M., 2015. Deep source model for Nevado del Ruiz Volcano, Colombia, constrained by interferometric synthetic aperture radar observations. Geophys. Res. Lett. 42 (12), 4816–4823.
Martone, M., Bräutigam, B., Rizzoli, P., Gonzalez, C., Bachmann, M., Krieger, G., 2012. Coherence evaluation of TanDEM-X interferometric data. ISPRS J. Photogramm. Remote Sens. 73, 21–29.
Milbert, D., 2002. VDatum transformation tool (new version 1.05), The GeoCommunitiy Spatial News.
Naranjo, J.L., Sigurdsson, H., Carey, S.N., Fritz, W., 1986. Eruption of the Nevado del Ruiz volcano, Colombia, on 13 November 1985: tephra fall and lahars. Science 233 (4767), 961–963.
Osmanoglu, B., Dixon, T.H., Wdowinski, S., 2014. Three-dimensional phase unwrapping for satellite radar interferometry, I: DEM generation. IEEE Trans. Geosci. Remote Sens. 52 (2), 1059–1075.
Papasaika, H., Kokiopoulou, E., Baltsavias, E., Schindler, K. and Kressner, D., 2011. Fusion of digital elevation models using sparse representations. In photogrammetric image analysis (pp. 171-184). Springer, Berlin, Heidelberg.
Parker, B., Milbert, D., Hess, K. and Gill, S., 2003, March. National VDatum–the implementation of a national vertical datum transformation database. In Proceeding from the US Hydro'2003 Conference (pp. 24-27).
Patra, A.K., Bauer, A.C., Nichita, C.C., Pitman, E.B., Sheridan, M.F., Bursik, M., Rupp, B., Webber, A., Stinton, A.J., Namikawa, L.M., Renschler, C.S., 2005. Parallel adaptive numerical simulation of dry avalanches over natural terrain. J. Volcanol. Geotherm. Res. 139 (1), 1–21.
Pierson, T.C., Janda, R.J., Thouret, J.C., Borrero, C.A., 1990. Perturbation and melting of snow and ice by the 13 November 1985 eruption of Nevado del Ruiz, Colombia, and consequent mobilization, flow and deposition of lahars. J. Volcanol. Geotherm. Res. 41 (1), 17–66.
Poland, M.P., 2014. Time-averaged discharge rate of subaerial lava at Kīlauea Volcano, Hawai'i, measured from TanDEM-X interferometry: implications for magma supply and storage during 2011–2013. Journal of Geophysical Research: Solid Earth 119 (7), 5464–5481.
Porcello, L.J., Massey, N.G., Innes, R.B., Marks, J.M., 1976. Speckle reduction in synthetic-aperture radars. JOSA 66 (11), 1305–1311.
Rabus, B., Eineder, M., Roth, A., Bamler, R., 2003. The shuttle radar topography mission - a new class of digital elevation models acquired by spaceborne radar. ISPRS J. Photogramm. Remote Sens. 57 (4), 241–262.
Reinartz, P., Müller, R., Hoja, D., Lehner, M. and Schroeder, M., 2005, June. Comparison and fusion of DEM derived from SPOT-5 HRS and SRTM data and estimation of forest heights. In Proc. EARSeL Workshop on 3D-Remote Sensing, Porto(Vol. 1).
Rizzoli, P., Martone, M., Gonzalez, C., Wecklich, C., Tridon, D.B., Bräutigam, B., Bachmann, M., Schulze, D., Fritz, T., Huber, M., Wessel, B., 2017. Generation and performance assessment of the global TanDEM-X digital elevation model. ISPRS J. Photogramm. Remote Sens. 132, 119–139.
Rossi, C., Minet, C., Fritz, T., Eineder, M., & Bamler, R., 2016. Temporal monitoring of subglacial volcanoes with TanDEM-X - Application to the 2014–2015 eruption within the Bárðarbunga volcanic system, Iceland. Remote Sens. Environ., 181, 186–197.
Rufino, G., Moccia, A., Esposito, S., 1998. DEM generation by means of ERS tandem data. IEEE Trans. Geosci. Remote Sens. 36 (6), 1905–1912.
Rusu, R.B. and Cousins, S., 2011, May. 3d is here: point cloud library (pcl). In robotics and automation (ICRA), 2011 IEEE International Conference on (pp. 1-4). IEEE.
Sansosti, E., Lanari, R., Fornaro, G., Franceschetti, G., Tesauro, M., Puglisi, G., Coltelli, M., 1999. Digital elevation model generation using ascending and descending ERS-1/ERS-2 tandem data. Int. J. Remote Sens. 20 (8), 1527–1547.
Schilling, S.P., 1998. LAHARZ; GIS programs for automated mapping of lahar-inundation hazard zones (No. 98–638). U.S. Geological Survey, Open-File Report 98–638.
Schilling, S.P., 2014. Laharz_py: GIS tools for automated mapping of lahar inundation hazard zones (No. 2014–1073). U.S. Geological Survey, Open-File Report 2014–1073.
Schindler, K., Papasaika-Hanusch, H., Schütz, S. and Baltsavias, E., 2011, September. Improving wide-area DEMs through data fusion–chances and limits. In proceedings of the photogrammetric week (Vol. 11, pp. 159-170).
Schultz, H., Riseman, E.M., Stolle, F.R. and Woo, D.M., 1999. Error detection and DEM fusion using self-consistency. In computer vision, 1999. The proceedings of the seventh IEEE international conference on (Vol. 2, pp. 1174-1181). IEEE.
Schuster, R.L., Highland, L., 2001. Socioeconomic and environmental impacts of landslides in the western hemisphere. U.S. Geological Survey, Open-File Report 01–0276.
SGC, Servicio Geológico Colombiano, 2015. Informe Técnico Mensual de la Actividad de Los Volcanes del Complejo volcánico Cerro Bravo Cerro Machín. Report in Spanish, Internal.
Smith, M.W., Carrivick, J.L., Quincey, D.J., 2016. Structure from motion photogrammetry in physical geography. Prog. Phys. Geogr. 40, 247–275.Strozzi, T., Werner, C., Wiesmann, A., Wegmuller, U., 2012. Topography mapping with a portable real-aperture radar interferometer. IEEE Geosci. Remote Sens. Lett., 9(2), 277–281.
Stevens, N.F., Manvilleb, V., Herona, D.W., 2003. The sensitivity of a volcanic flow model to digital elevation model accuracy: experiments with digitised map contours and interferometric SAR at Ruapehu and Taranaki volcanoes, New Zealand. J. Volcanol. Geotherm. Res. 119 (1–4), 89–105.
Strozzi, T., Werner, C., Wiesmann, A., Wegmuller, U., 2012. Topography mapping with a portable real-aperture radar interferometer. IEEE Geosci. Remote Sens. Lett. 9 (2), 277–281.
Tachikawa, T., Hato, M., Kaku, M. and Iwasaki, A., 2011, July. Characteristics of ASTER GDEM version 2. In geoscience and remote sensing symposium (IGARSS), 2011 IEEE international (pp. 3657-3660). IEEE.
Tadono, T., Ishida, H., Oda, F., Naito, S., Minakawa, K. and Iwamoto, H., 2014. Precise global DEM generation by ALOS PRISM. ISPRS annals of the photogrammetry, Remote Sensing and Spatial Information Sciences, 2(4), p. 71.
Toutin, T., 2004. Comparison of stereo-extracted DTM from different high-resolution sensors: SPOT-5, EROS-A, IKONOS-II, and QuickBird. IEEE Trans. Geosci. Remote Sens. 42 (10), 2121–2129.
Toutin, T., 2008. ASTER DEMs for geomatic and geoscientific applications: a review. Int. J. Remote Sens. 29 (7), 1855–1875.
Turner, N.R., Perroy, R.L., Hon, K., 2017. Lava flow hazard prediction and monitoring with UAS: a case study from the 2014–2015 Pāhoa lava flow crisis, Hawai 'i. J. Appl. Volcanol. 6, 17.
Van Niel, T.G., McVicar, T.R., Li, L., Gallant, J.C., Yang, Q., 2008. The impact of misregistration on SRTM and DEM image differences. Remote Sens. Environ. 112 (5), 2430–2442.
Vargas, C.A., Koulakov, I., Jaupart, C., Gladkov, V., Gomez, E., El Khrepy, S., Al-Arifi, N., 2017. Breathing of the Nevado del Ruiz volcano reservoir, Colombia, inferred from repeated seismic tomography. Sci. Rep. 7, 46094.
Voytenko, D., Dixon, T.H., Howat, I.M., Gourmelen, N., Lembke, C., Werner, C.L., De La Peña, S., Oddsson, B., 2015. Multi-year observations of Breiðamerkurjökull, a marine-terminating glacier in southeastern Iceland, using terrestrial radar interferometry. J. Glaciol. 61 (225), 42–54.
Wadge, G., Cole, P., Stinton, A., Komorowski, J.C., Stewart, R., Toombs, A.C., Legendre, Y., 2011. Rapid topographic change measured by high-resolution satellite radar at Soufriere Hills Volcano, Montserrat, 2008–2010. J. Volcanol. Geotherm. Res. 199 (1–2), 142–152.
Warmerdam F., 2008. The Geospatial Data Abstraction Library. In: Hall G.B., Leahy M.G. (eds) Open Source Approaches in Spatial Data Handling. Advances in Geographic Information Science, vol 2. Springer, Berlin, Heidelberg.
Werner, C., Wegmüller, U., Strozzi, T. and Wiesmann, A., 2000. Gamma SAR and interferometric processing software. In Proceedings of the ers-envisat symposium, Gothenburg, Sweden (Vol. 1620, p. 1620).
Werner, C., Strozzi, T., Wiesmann, A. and Wegmüller, U., 2008, May. GAMMA's portable radar interferometer. In Proc. 13th FIG Symp. Deform. Meas. Anal (pp. 1-10).
Westoby, M.J., Brasington, J., Glasser, N.F., Hambrey, M.J., Reynolds, J.M., 2012. 'Structure-from-motion' photogrammetry: A low-cost, effective tool for geoscience applications. Geomorphology 179, 300–314.
Wunderman, R. (ed.), 2012. Global Volcanism Program. Report on Nevado del Ruiz (Colombia). Bulletin of the Global Volcanism Network, 37:8. Smithsonian Institution. doi:https://doi.org/10.5479/si.GVP.BGVN201208-351020.
Xie, S., Dixon, T.H., Voytenko, D., Holland, D.M., Holland, D., Zheng, T., 2016. Precursor motion to iceberg calving at Jakobshavn Isbræ, Greenland, observed with terrestrial radar interferometry. J. Glaciol. 62 (236), 1134–1142.
Xie, S., Dixon, T.H., Voytenko, D., Deng, F., Holland, D.M., 2018. Grounding line migration through the calving season at Jakobshavn Isbræ, Greenland, observed with terrestrial radar interferometry. Cryosphere 12 (4), 1387–1400.
Xie, S., Dixon, T.H., Holland, D.H., Voytenko, D., Vaňková, I., 2019. Rapid iceberg calving following removal of tightly packed pro-glacial mélange. Nat. Commun. 10, 3250. https://doi.org/10.1038/s41467-019-10908-4.
Yang, Q., Zhao, W., Dixon, T.H., Amelung, F., Han, W.S., Li, P., 2015. InSAR monitoring of ground deformation due to CO2 injection at an enhanced oil recovery site, West Texas. International Journal of Greenhouse Gas Control 41, 20–28.
Zebker, H.A., Goldstein, R.M., 1986. Topographic mapping from interferometric synthetic aperture radar observations. Journal of Geophysical Research: Solid Earth 91 (B5), 4993–4999.
Zhou, Y., Zhou, C., Deng, F., Dongchen, E., Liu, H., Wen, Y., 2015. Improving InSAR elevation models in Antarctica using laser altimetry, accounting for ice motion, orbital errors and atmospheric delays. Remote Sens. Environ. 162, 112–118.
Zink, M., Krieger, G., Fiedler, H., Hajnsek, I., Moreira, A., 2008. The TanDEM-X mission concept. In Synthetic Aperture Radar (EUSAR), 2008 7th European Conference on (pp. 1-4). VDE.